Structural basis of mitochondrial membrane bending by I-II-III_2-IV_2 supercomplex

Alexander Mühleip[1†], Rasmus Kock Flygaard[1,2†], Outi Haapanen[3], Rozbeh Baradaran[1,4], Thomas Gruhl[5], Victor Tobiasson[1], Amandine Maréchal[5,6], Vivek Sharma[3,7], Alexey Amunts[1*]

[1] Science for Life Laboratory, Department of Biochemistry and Biophysics, Stockholm University, 17165 Solna, Sweden.

[2] Current address: Department of Molecular Biology and Genetics, Danish Research Institute of Translational Neuroscience - DANDRITE, Nordic EMBL Partnership for Molecular Medicine, Aarhus University, 8000 Aarhus C, Denmark.

[3] Department of Physics, University of Helsinki, 00014 Helsinki, Finland.

[4] Current address: MRC Laboratory of Molecular Biology, Cambridge, United Kingdom.

[5] Institute of Structural and Molecular Biology, Birkbeck College, London, WC1E 7HX, UK.

[6] Institute of Structural and Molecular Biology, University College London, London, WC1E 6BT, UK.

[7] HiLIFE Institute of Biotechnology, University of Helsinki, 00014 Helsinki, Finland.

† These authors contributed equally to this work.

* Correspondence to: amunts@scilifelab.se.

Mitochondrial energy conversion requires an intricate architecture of the inner mitochondrial membrane[1]. Here we show that in ciliates, the membrane curvature is provided by a supercomplex containing all four respiratory chain components. We report cryo-electron microscopy and cryo-tomography structures of the supercomplex that comprises 150 different proteins and 311 bound lipids, forming a stable 5.8-megadalton assembly. Due to subunit acquisition and extension, complex I associates with a complex IV dimer, generating a wedge-shaped gap that serves as a binding site for complex II. Together with a tilted complex III dimer association, it results in a curved membrane region. Using molecular dynamics simulations, we demonstrate that the divergent supercomplex actively contributes to the membrane curvature induction and cristae tubulation. Our findings explain how the architecture of the native I-II-III_2-IV_2 supercomplex reflects the functional specialization of bioenergetics by shaping the membrane.

Mitochondrial energy conversion requires an electron transport chain (ETC) that generates a membrane potential across the inner mitochondrial membrane to drive the essential adenosine triphosphate (ATP) formation by F_1F_o-ATP synthase. The ETC consists of four multi-subunit membrane complexes: complex I (CI, NADH:ubiquinone oxidoreductase), complex II (CII, succinate:ubiquinone oxidoreductase), complex III (CIII, cytochrome bc1 complex) and complex IV (CIV, cytochrome c oxidase). Structural analyses have shown that these components can organize into supercomplexes containing CI, CIII dimer ($CIII_2$), and CIV[1]. CII transfers electrons from succinate via its covalently bound flavin adenine dinucleotide (FAD) and iron-sulfur clusters to ubiquinone (UQ) and is also a component of the TCA cycle, making a functional link between the two central metabolic pathways[2]. Although CII has been suggested to interact with mammalian ETC complexes[3-7], it was not experimentally found as a part of any characterized supercomplex. In addition, for the bioenergetic process to occur, a specific topology of the cristae membranes that form functionally distinct high-potential compartments is critical[8]. An established mechanism for maintenance of such a topology relies on oligomerization of ATP synthase and its specific interplay with lipids[9-13]. In ciliates, the inner mitochondrial membrane is organized as tubular cristae, which cannot be explained by the helical row assembly of ATP synthase alone[11,14,15].

We purified the intact respiratory supercomplex from the ciliate protist *Tetrahymena thermophila* mitochondria and determined its structure by single-particle cryo–electron microscopy (cryo-EM) (Extended Data Fig. 1 and SI Table 1). At an overall resolution of 2.9 Å, the structure revealed CI, CII, $CIII_2$, and CIV dimer (CIV_2) associated into a 5.8-megadalton supercomplex (Fig. 1). When viewed along the membrane plane, the assembly of more than 300 transmembrane helices displays a bent shape, indicating that the accommodating membrane adopts a local curvature with radius of ~20 nm (Fig. 1). Focused refinements resolved individual structures that together form an assembly of 150 different protein subunits and 311 bound lipids (Extended Data Figs. 1 and 2, SI Tables 1 and 2). CIV_2 is associated with the long side of the membrane region of CI, opposite to $CIII_2$. This arrangement is markedly different compared to known mammalian supercomplexes[16,17] and correlates with the acquisition of four ciliate-specific CI subunits that would clash with the position of CIV as seen in mammals (Fig. 1D, Extended Data Fig. 3, SI Fig. 1). CII is anchored in between CI and CIV, highlighting the unique architecture and composition of the native supercomplex (Fig.1). To further substantiate the occurrence of a functional supercomplex, we performed in-gel activity assays. These confirmed the presence of functional electron-transfer systems in CI, CII and CIV with activities mapping to a common high molecular weight band, which we assign as the intact supercomplex (SI Fig. 2).

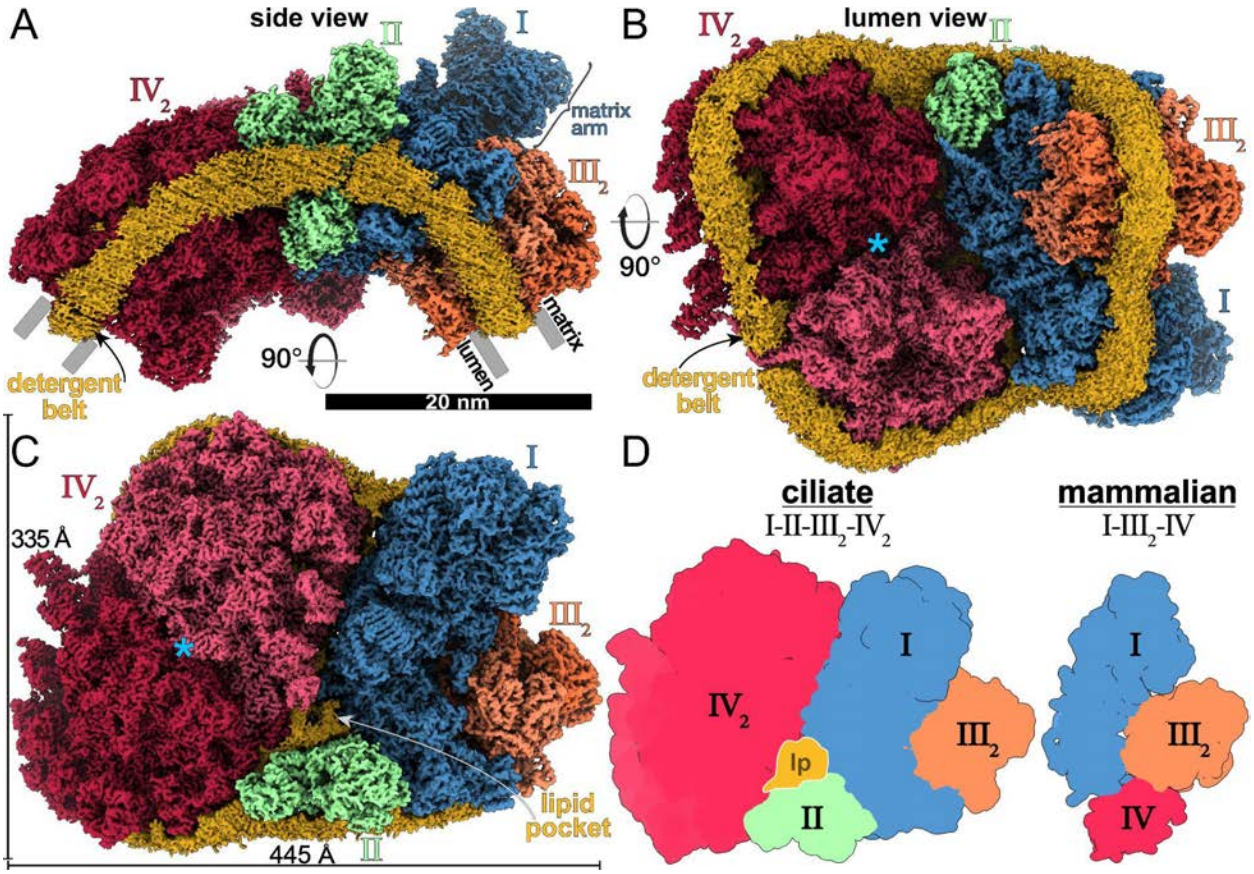

Fig. 1. The supercomplex contains all four ETC components. (A) Side view of the supercomplex density showing the curved detergent micelle (yellow). **(B)** Lumenal view illustrates how the complexes CI, CII and CIV_2 stabilize each other. Blue asterisk indicates the symmetry axis of CIV_2. **(C)** Matrix view shows CII binding in a wedge between CI and CIV_2, resulting in the enclosure of a lipid pocket (lp). **(D)** Architecture comparison of the ciliate supercomplex (this study) with mammalian respirasome (PDB 5J4Z) highlighting a different location of CIV_2 that is correlated with acquisition of CI subunits that stabilize $CIII_2$.

CIV_2 is the most divergent of the four ETC complexes (Extended Data Figs. 4 and 5, SI Fig. 3). We modeled 105 lipids, four previously unobserved ubiquinones and 53 protein chains per monomer, of which four are mitochondrially encoded (Extended Data Fig. 2C-F, Extended Data Fig. 6). We found that two of those subunits, previously annotated as ciliate-specific Ymf67 and Ymf68/COX3 represent complementary protein fragments, with coding genes split in the mt-genome by $tRNA^{Trp}$ gene insertion (Extended Data Fig. 7). Each fragment has subsequently been extended by over 400 and 200 residues respectively. Together, they form a functional COX3 (COX3a, COX3b), including the conserved seven-TM-helix fold (Extended Data Fig. 7A, SI Fig. 3). In our structure, COX3a and COX3b extend throughout the CIV membrane region, and COX3b has evolved interactions with CI subunits on the matrix side, thereby mediating the supercomplex assembly (Fig. 2, A and B, Extended Data Fig. 7A). Particularly, COX3b forms a

contact with a peripheral amphipathic helix of NDUCA1, which is part of a zinc-free γ-carbonic anhydrase heterotrimer (γ-CA) (Fig. 2D). The γ-CA was previously reported in viridiplantae and ciliates (both diaphoretickes)[7,18], and our structure demonstrates that it acts as a structural scaffold within the supercomplex architecture. Another CI-IV contact at the same site involves COXTT2 with an N-terminal globlin-like domain that interacts with NDUFA3 and was not resolved in the individual CIV_2 structure[7], suggesting that it becomes ordered to mediate supercomplex formation (Fig. 2A and D, Extended Data Fig. 6A). Interestingly, the second major interaction site at the CI-IV interface, which is on the lumenal side of the membrane also involves a fragmented protein subunit, this time from CI (Extended Data Fig. 7C and D). Consistent with the observation with respect to the protein splitting in CIV, here we modeled the N-terminal extension of ND5 fragment (ND5a), as well as the newly identified protein subunit NDUTT16 (from CI) (Fig. 2 A-C). NDUTT16 engages in interactions with at least four subunits of CIV, as well as an interfacial CIV heme group (Fig. 2C).

Our finding of the split core subunits gaining a capacity of establishing inter-complex contacts to stabilise the supercomplex that curves the membrane suggests an evolutionary mechanism by which gene fragmentation, followed by its expansion can convey subunit function. Overall, the $CI\text{-}IV_2$ interface involves 25 subunits, forming an extensive buried interface of ~2,300 $Å^2$ with a curved membrane region (Fig. 2, A and B).

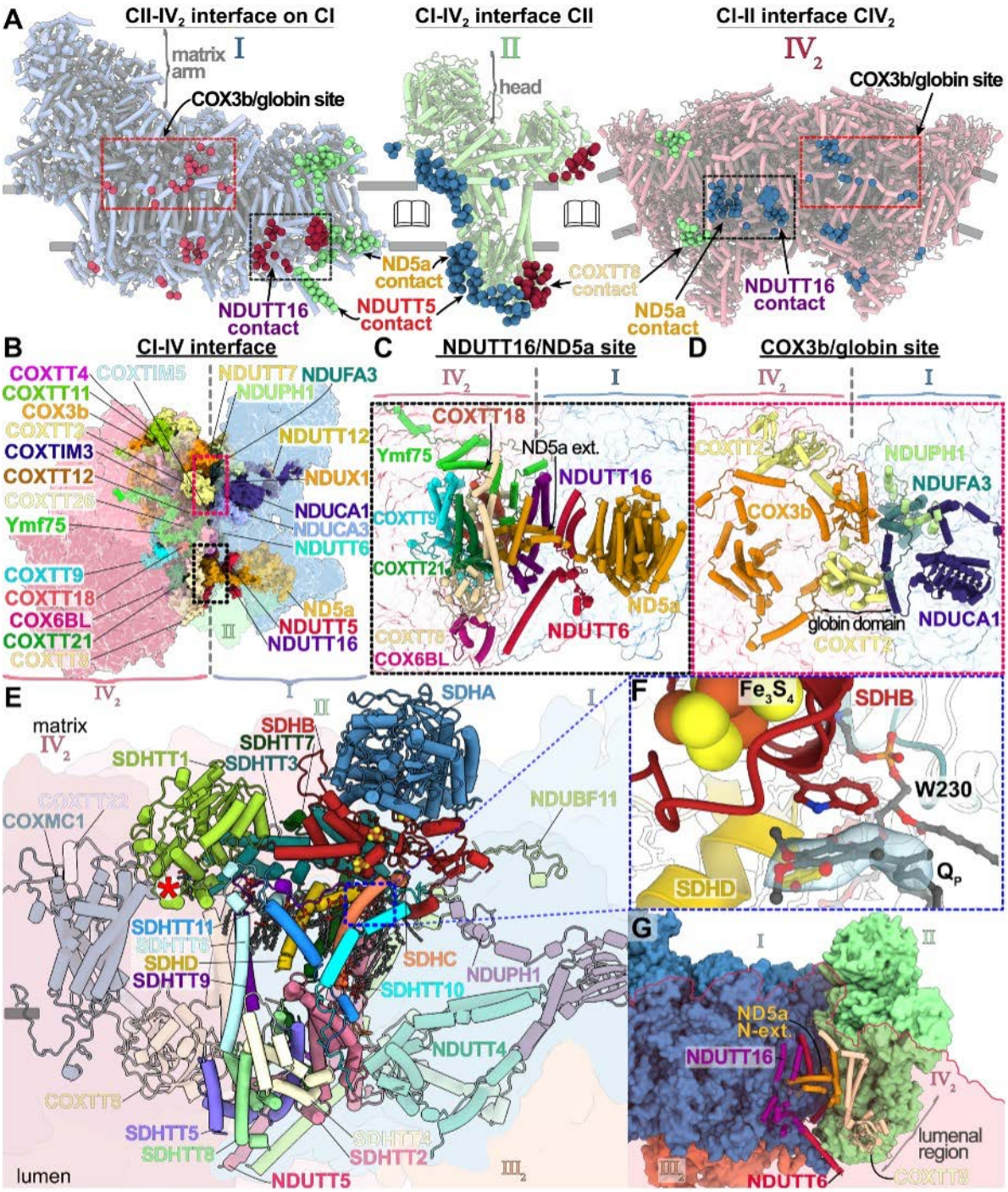

Fig. 2. The CI-CIV association, and binding of CII. (A) Contact sites of CI with CII-IV_2 (left), CII with CI-IV_2 (middle), CIV_2 with CI-II (right). Interactions are shown as spheres (CI blue, CII green, CIV_2 red/dark and pink). Only one CIV monomer interacts with CII. Main interaction sites are indicated. **(B)** The CI-IV_2 interacting subunits are shown in colored surfaces. **(C)** NDUTT16/ND5a contact site. **(D)** COX3b/NDUCA1 contact site. **(E)** CII binding to subunits of CI-IV (transparent), asterisk marks C-type heme. **(F)** CII contains a bound proximal ubiquinone. **(G)** CI, CII and CIV are connected together via the membrane and lumenal regions.

116 Tt-CII binds in a wedge-shaped gap formed by CI-CIV in our structure (Fig. 1, A-C). In addition
117 to the four canonical subunits (SDHA-D), it is composed of 11 ciliate-specific subunits
118 SDHTT1-11 (Fig. 2E, Extended Data Fig. 8A). The matrix module SDHA and SDHB forms a
119 conserved head region, containing both the covalently bound FAD and three iron-sulfur clusters
120 (Fig. 2F, Extended Data Fig. 8B). The membrane anchor is formed by two small subunits SDHC
121 (7 kDa) and mitochondria-encoded SDHD (5 kDa), which could only be assigned by locating
122 topologically conserved transmembrane helices in the map (Extended Data Fig. 8 A,C,D). At the
123 lumen, a ~70-kDa module (SDHTT2, 4, 5, and 8) anchors CII to CI-IV (Fig. 2E, Extended Data
124 Fig. 8A). SDHTT5 interacts with a helix of NDUTT5 protruding from the membrane arm of CI,
125 and with the Surf1-like protein subunit COXTT8 (CIV) (Fig. 2, A and E). Remarkably, at the
126 same position COXTT8 interacts with CI via the N-terminal NDA5a extension, and with Ymf75,
127 COXTT27 and COXTT18 at the CIV dimer interface. Thus, the three complexes are connected
128 together in the lumen (Fig. 2G).

129 In between SDHB and SDHD, we identified a ligand which we assign as the proximal ubiquinol
130 (Q_p) (Fig. 2F)[19,20]. On the matrix side, the 36-kDa soluble subunit SDHTT1 contains a bis-
131 histidine C-type heme group covalently bound by a single cysteine residue (Extended Data Fig.
132 8E). Although it is exposed to the membrane region, at a distance of ~60 Å to the Fe_3S_4 cluster,
133 the non-canonical heme-c is located too far to participate in direct CII electron transfer (Fig. 2F,
134 Extended Data Fig. 8A,E). To elucidate the presence of additional heme groups in the
135 supercomplex, we recorded absorption spectra of the purified sample (Extended Data Fig. 9).
136 Deconvolution of the merged absorption bands of B- and C-type hemes indicated the presence of
137 at least one additional heme group with absorption at 556 nm.

138 The presence of a functional ETC with CII is consistent with previous observations that
139 *T. thermophila* can utilize succinate to drive cellular respiration[21]. Our native structure with
140 bound CII, which contributes to the ubiquinol pool, demonstrates that supercomplex assembly is
141 not limited to proton-pumping respiratory chain components (CI, CIII, CIV). Beyond decreasing
142 cytochrome-c transfer distance[22], this suggests a potential role of supercomplex formation in
143 mediating increased ubiquinone diffusion, as suggested in analogous membrane systems with
144 high protein-lipid ratios[23,24]. Furthermore, the tubular membrane morphology may require the
145 anchoring of CII into the curved supercomplex to retain it in the functionally relevant cristae,
146 preventing diffusion into flat membrane regions.

147 $CIII_2$ in our structure is tilted with respect to CI by 37° (Fig. 3A and SI Fig. 4). This tilted
148 arrangement offsets the transmembrane region, consistent with its curved membrane
149 environment. The interface involves 20 subunits and 19 bound native lipids interacting through
150 the matrix, transmembrane and luminal sides (Extended Data Fig. 10). When compared to the
151 mammalian counterpart, $CIII_2$ is rotated by 41° and shifted ~14 Å due to acquisition of four CI
152 subunits, as well as the CIII subunit UQCRTT1 (Fig. 3A and Extended Data Fig. 10B,C)[16,25-27].
153 This arrangement results in a specific CI-$CIII_2$ contact with one copy of Rieske iron sulfur
154 protein (UQCRFS1) interacting with the CI membrane arm (Fig. 3B). The interaction site is

155 further augmented by a hitherto unidentified protein UQCRTT3, which interacts with the luminal
156 head domain of UQCRFS1 and wedges in between the interface to CYC1 (Fig. 3B).

157 We traced the membrane-accessible UQ-tunnel, lined by UQCR10 and ciliate-specific subunit
158 UQCRTT2 (Fig. 3C), leading to the COB heme b_H, where density for a bound (semi)-ubiquinone
159 was observed in the Q_i site (Fig. 3D)[28]. Furthermore, we observed map density features close to
160 the two heme b_L groups which likely correspond to ubiquinols bound at the Q_o sites (Fig. 3D and
161 E). The distances between the Q_o site, heme b_L and heme b_H within one CIII monomer are
162 consistent with those observed in mammalian $CIII_2$ (SI Fig. 5A), with the two heme b_L molecules
163 in COB being bridged by a non-canonical UQ (SI Fig. 5B and supplementary text). We detected
164 density for two copies of the flexible UQCRFS1 head domain (Extended Data Fig. 11), which
165 contrasts with a recent work that found only the head domain proximal to the CI quinone tunnel
166 to display flexibility, whereas the distal domain at the CI interface was proposed to be
167 nonfunctional in electron transport[7]. Using focused 3D classification for the distal UQCRFS1
168 head domain (Extended Data Fig. 11B), we then identified two classes likely representing the
169 extremes of the head domain movement from the B state where the Fe_2S_2 cluster is distanced
170 from heme c_1 to the C state where the Fe_2S_2 cluster is closest (Fig. 3F,G, Extended Data Fig.
171 11C,D)[29,30]. This movement of the UQCRFS1 head domain is coupled to conformational changes
172 in the unidentified UQCRTT3 protein, thus suggesting a potential role for this subunit in
173 regulation of $CIII_2$ activity (Extended Data Fig. 11D). Thus, our observation of the distal
174 UQCRFS1 head domain flexibility, together with the heme b_L-wedged UQ, suggests that
175 functional symmetry is maintained in the ciliate $CIII_2$ despite deviation from the structural
176 symmetry.

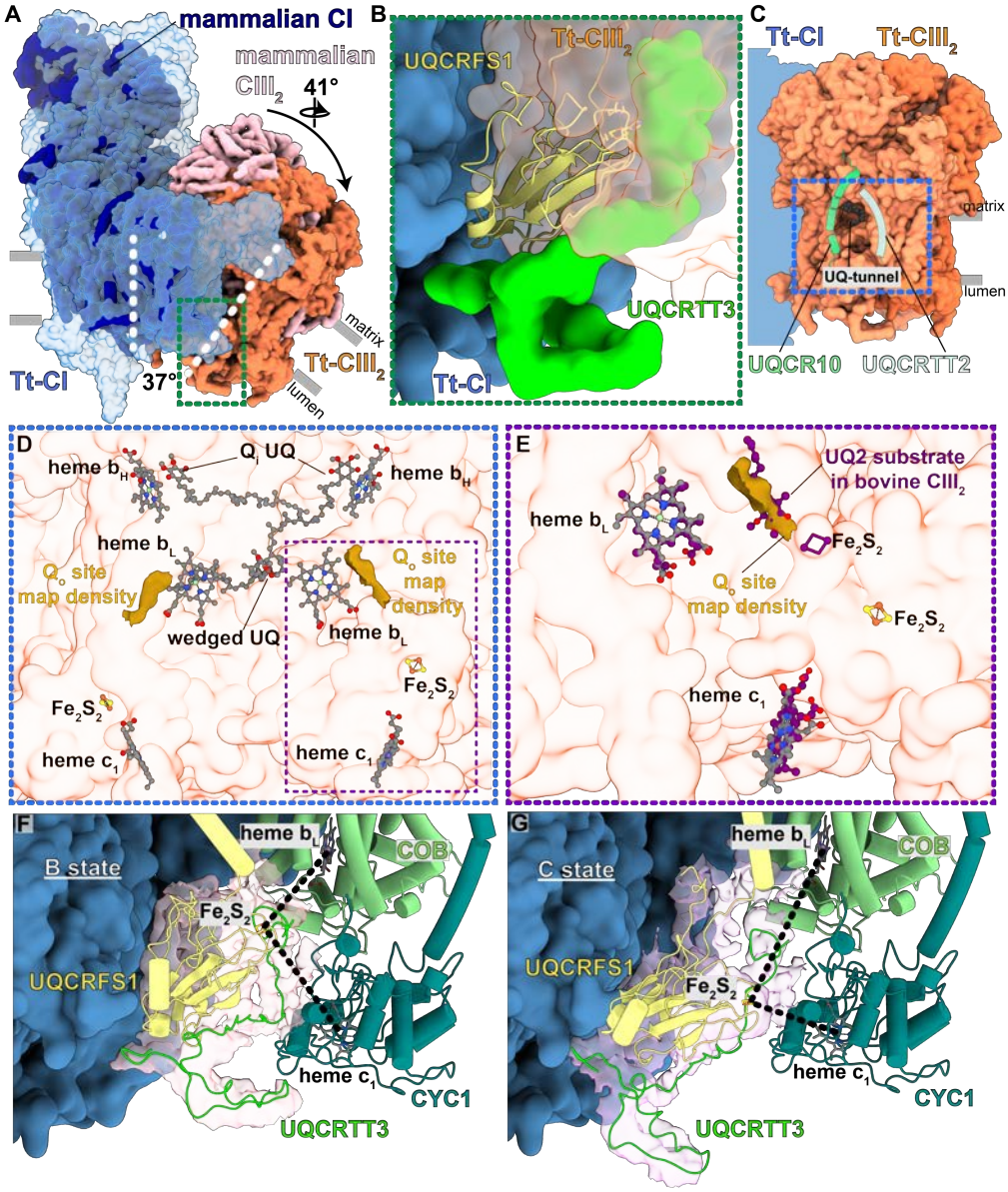

Fig. 3. Altered CI-CIII$_2$ interface maintains functional symmetry of CIII$_2$. (A) Superposition of Tt-CI-CIII$_2$ with mammalian CI-CIII$_2$ (PDB 5J4Z) shows that Tt-CIII$_2$ is tilted, rotated and displaced with respect to the CI membrane arm, as indicated by dashed lines and arrows due to acquisition of new proteins. Green box view is shown in B. **(B)** Tilted Tt-CIII$_2$ results in an interaction between UQCRFS1 and CI membrane arm together with UQCRTT3. **(C)** Tt-CIII$_2$ shows a membrane-accessible tunnel extending to the COB Q_i sites. Blue box view is shown in D. **(D)** The Q_i ubiquinones are located close to heme b_H, with one ubiquinone wedged in between the two heme b_L molecules. The density map of Tt-CIII$_2$ shows two features corresponding to Q_o sites. Purple box view is shown in E. **(E)** The Q_o site density overlaps with ubiquinol in bovine CIII$_2$ structure (PDB 1NTZ). **(F,G)** 3D maps showing B state (F) and C state (G) conformations of UQCRFS1 and UQCRTT3. Only COB and CYC1 proteins are shown for clarity, highlighting distances of Fe_2S_2 to heme c_1 and b_L (black dashes).

190 To investigate if the membrane-bending capacity of the supercomplex is biologically relevant,
191 we performed electron cryo-tomography of isolated mitochondrial membranes. Cryo-tomograms
192 revealed ~40-nm tubular cristae densely packed with helical ATP synthase rows and
193 supercomplexes, identified by the conspicuous CI matrix arm (Fig. 4A). To elucidate the
194 supercomplex architecture *in situ*, we performed subtomogram averaging and obtained a map at
195 28 Å resolution (Extended Data Fig. 1E). The subtomogram average confirmed the presence of
196 the supercomplex, which fits our atomic model (Extended Data Fig. 1F). The appearance of a
197 tubular membrane density in the subtomogram average suggests that the supercomplex adopts a
198 preferred orientation, with its CI-IV_2 interface approximately aligned with the long axis of the
199 tube (Fig. 4B). Furthermore, the curved membrane region of the supercomplex subtends an angle
200 of ~130°, indicating that it contributes to the tubular shape of the cristae.

201 To elucidate the membrane-shaping activity of the supercomplex, we performed coarse-grained
202 molecular dynamics simulations. When placed into a planar lipid bilayer, the supercomplex
203 induces a curved membrane topology, displacing the membrane by 18 nm from the original
204 plane (Fig. 4C, SI Video 1). Furthermore, the annular lipid shell surrounding the complex in the
205 equilibrated system displays a highly curved architecture, supportive of an active role in
206 membrane curvature induction (Fig. 4D, SI Video 2). Additionally, we observed lipid pockets in
207 the transmembrane interfaces between subcomplexes, which suggests that their maintenance is
208 crucial for the supercomplex integrity (Extended Data Fig. 2A,B).

209 Our results indicate a cristae-shaping mechanism involving both the respiratory supercomplex
210 and the ATP synthase to produce membrane tubulation. It serves the function of confining a
211 narrow cristae diameter of around 40 nm, which allows tight cristae packing, thereby increasing
212 the surface area of the bioenergetic membrane. thus favouring ATP synthesis. This membrane-
213 shaping organization of the respiratory supercomplex is markedly different from the mammalian
214 homolog, which resides in the flat crista regions, thereby generating a spatial segregation from
215 ATP synthase[31]. Furthermore, the observed colocalization of the four respiratory complexes
216 would contribute to a directional proton gradient inside the cristae. Because the crista lumen
217 displays the highest membrane potential, with every crista representing an independent
218 functional compartment[32], the restriction of the cristae diameter likely serves to minimize the
219 lumenal compartment, thereby ensuring that proton translocation results in an increased local
220 membrane potential and ultimately favouring ATP synthesis.

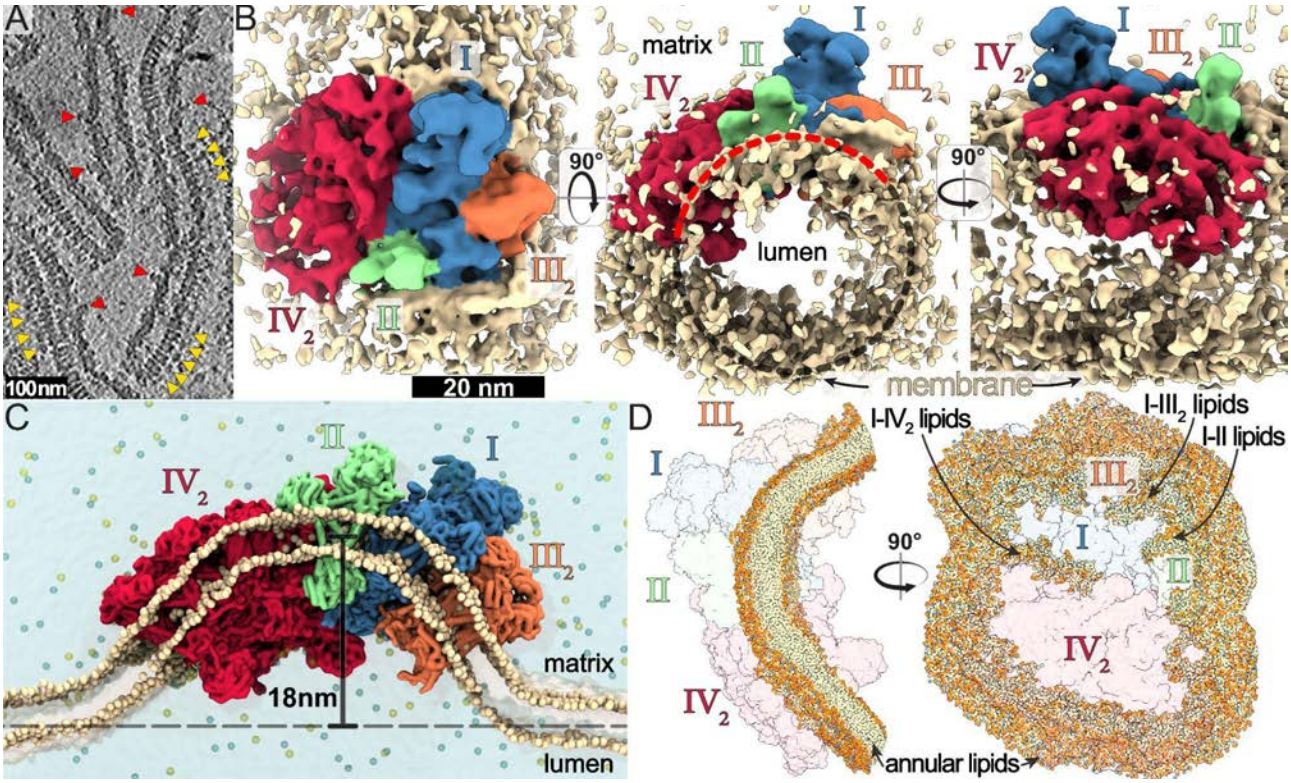

Figure 4: *In-situ* structure and molecular dynamics of the I-II-III$_2$-IV$_2$ supercomplex indicate a membrane bending function. (A) Cryo-tomographic slice of tubular cristae with ~40-nm diameter. ATP synthase and supercomplex marked with yellow and red arrowheads. **(B)** Subtomogram average of the I-II-III$_2$-IV$_2$ supercomplex revealing a preferred orientation in tubular membranes and an arc-shaped structure subtending ~130° (red dashes). **(C)** Coarse-grained MD simulation showing that the arched membrane region of the supercomplex generates a significant membrane curvature, resulting in 18-nm local displacement of the membrane from the bilayer plane. **(D)** MD simulation reveals the curved structure of the annular lipid shell surrounding the supercomplex, as well as lipid-filled subcomplex interfaces.

References

1. N. J. Caruana, D. A. Stroud, The road to the structure of the mitochondrial respiratory chain supercomplex. *Biochem Soc Trans* **48**, 621-629 (2020).
2. A. Bezawork-Geleta, J. Rohlena, L. Dong, K. Pacak, J. Neuzil, Mitochondrial Complex II: At the Crossroads. *Trends Biochem Sci* **42**, 312-325 (2017).
3. R. Acin-Perez, P. Fernandez-Silva, M. L. Peleato, A. Perez-Martos, J. A. Enriquez, Respiratory active mitochondrial supercomplexes. *Mol Cell* **32**, 529-539 (2008).
4. C. Jiang *et al.*, Regulation of Mitochondrial Respiratory Chain Complex Levels, Organization, and Function by Arginyltransferase 1. *Front Cell Dev Biol* **8**, 603688 (2020).
5. E. Lapuente-Brun *et al.*, Supercomplex assembly determines electron flux in the mitochondrial electron transport chain. *Science* **340**, 1567-1570 (2013).
6. E. A. Schon, N. A. Dencher, Heavy breathing: energy conversion by mitochondrial respiratory supercomplexes. *Cell Metab* **9**, 1-3 (2009).

7. L. Zhou, M. Maldonado, A. Padavannil, F. Guo, J. A. Letts, Structures of Tetrahymena's respiratory chain reveal the diversity of eukaryotic core metabolism. *Science*, eabn7747 (2022).
8. L. Colina-Tenorio, P. Horten, N. Pfanner, H. Rampelt, Shaping the mitochondrial inner membrane in health and disease. *J Intern Med* **287**, 645-664 (2020).
9. T. B. Blum, A. Hahn, T. Meier, K. M. Davies, W. Kühlbrandt, Dimers of mitochondrial ATP synthase induce membrane curvature and self-assemble into rows. *Proc Natl Acad Sci U S A*, (2019).
10. A. Mühleip, S. E. McComas, A. Amunts, Structure of a mitochondrial ATP synthase with bound native cardiolipin. *eLife* **8**, (2019).
11. R. Kock Flygaard, A. Mühleip, V. Tobiasson, A. Amunts, Type III ATP synthase is a symmetry-deviated dimer that induces membrane curvature through tetramerization. *Nat Commun*, (2020).
12. G. Pinke, L. Zhou, L. A. Sazanov, Cryo-EM structure of the entire mammalian F-type ATP synthase. *Nat Struct Mol Biol*, (2020).
13. A. Mühleip *et al.*, ATP synthase hexamer assemblies shape cristae of *Toxoplasma* mitochondria. *Nat Commun* **12**, 120 (2021).
14. A. W. Mühleip *et al.*, Helical arrays of U-shaped ATP synthase dimers form tubular cristae in ciliate mitochondria. *Proc Natl Acad Sci USA* **113**, 8442-8447 (2016).
15. R. D. Allen, C. C. Schroeder, A. K. Fok, An investigation of mitochondrial inner membranes by rapid-freeze deep-etch techniques. *J Cell Biol* **108**, 2233-2240 (1989).
16. J. Gu *et al.*, The architecture of the mammalian respirasome. *Nature* **537**, 639-643 (2016).
17. R. Guo, S. Zong, M. Wu, J. Gu, M. Yang, Architecture of Human Mitochondrial Respiratory Megacomplex I2III2IV2. *Cell* **170**, 1247-1257 e1212 (2017).
18. N. Klusch, J. Senkler, O. Yildiz, W. Kuhlbrandt, H. P. Braun, A ferredoxin bridge connects the two arms of plant mitochondrial complex I. *Plant Cell* **33**, 2072-2091 (2021).
19. C. Hagerhall, Succinate: quinone oxidoreductases. Variations on a conserved theme. *Biochim Biophys Acta* **1320**, 107-141 (1997).
20. F. Sun *et al.*, Crystal structure of mitochondrial respiratory membrane protein complex II. *Cell* **121**, 1043-1057 (2005).
21. P. Balabaskaran Nina *et al.*, Highly divergent mitochondrial ATP synthase complexes in Tetrahymena thermophila. *PLoS Biol* **8**, e1000418 (2010).
22. J. Berndtsson *et al.*, Respiratory supercomplexes enhance electron transport by decreasing cytochrome c diffusion distance. *EMBO Rep* **21**, e51015 (2020).
23. I. G. Tremmel, H. Kirchhoff, E. Weis, G. D. Farquhar, Dependence of plastoquinol diffusion on the shape, size, and density of integral thylakoid proteins. *Biochim Biophys Acta* **1607**, 97-109 (2003).
24. H. Kirchhoff, Diffusion of molecules and macromolecules in thylakoid membranes. *Biochim Biophys Acta* **1837**, 495-502 (2014).
25. J. A. Letts, K. Fiedorczuk, L. A. Sazanov, The architecture of respiratory supercomplexes. *Nature* **537**, 644-648 (2016).
26. T. Althoff, D. J. Mills, J. L. Popot, W. Kuhlbrandt, Arrangement of electron transport chain components in bovine mitochondrial supercomplex I1III2IV1. *EMBO J* **30**, 4652-4664 (2011).
27. M. Wu, J. Gu, R. Guo, Y. Huang, M. Yang, Structure of Mammalian Respiratory Supercomplex I1III2IV1. *Cell* **167**, 1598-1609 e1510 (2016).

28. X. Gao *et al.*, Structural basis for the quinone reduction in the bc1 complex: a comparative analysis of crystal structures of mitochondrial cytochrome bc1 with bound substrate and inhibitors at the Qi site. *Biochemistry* **42**, 9067-9080 (2003).
29. Z. Zhang *et al.*, Electron transfer by domain movement in cytochrome bc1. *Nature* **392**, 677-684 (1998).
30. S. Rajagukguk *et al.*, Effect of mutations in the cytochrome b ef loop on the electron-transfer reactions of the Rieske iron-sulfur protein in the cytochrome bc1 complex. *Biochemistry* **46**, 1791-1798 (2007).
31. K. M. Davies *et al.*, Macromolecular organization of ATP synthase and complex I in whole mitochondria. *Proc Natl Acad Sci U S A* **108**, 14121-14126 (2011).
32. D. M. Wolf *et al.*, Individual cristae within the same mitochondrion display different membrane potentials and are functionally independent. *EMBO J* **38**, e101056 (2019).

Methods

Purification of *T. thermophila* supercomplex

T. thermophila cells were grown at the temperature of 36 °C and harvested as previously described[11], and cell pellets were resuspended in homogenization buffer (20 mM Hepes/KOH pH 7.5, 350 mM D-mannitol, 5 mM EDTA, 1x protease-inhibitor tablet) and lysed in a Dounce homogenizer on ice. Intact mitochondria were isolated first by differential centrifugation of the lysate and finally on a discontinuous sucrose gradient with 15%, 23%, 32% and 60% w/v sucrose in buffer SEM (20 mM Hepes/KOH pH 7.5, 250 mM sucrose, 1 mM EDTA) at 14,1371 xg for 60 min and 4°C in an SW28 rotor. Intact mitochondria sedimented to the interface between 32% and 60% sucrose and were collected from the gradient, snap-frozen in liquid nitrogen and stored at -80°C. The isolated mitochondria were lysed in buffer A (25 mM Hepes/KOH pH 7.5, 25 mM KCl, 5 mM $MgCl_2$, 4% w/v digitonin) for one hour on ice. This procedure was previously confirmed as a gentle solubilization method. Following mitochondrial membrane solubilization, cleared lysate was placed on a sucrose cushion (25 mM Hepes/KOH pH 7.5, 25 mM KCl, 5 mM $MgCl_2$, 0.1% w/v digitonin, 30% w/v sucrose) in Ti70 tubes and centrifuged at 164,685 xg for 3 h. The pellet was gently washed and finally resuspended in buffer D (25 mM Hepes/KOH pH 7.5, 25 mM KCl, 5 mM $MgCl_2$, 0.1% w/v digitonin). Prior to loading sample material on a size exclusion chromatography column, larger aggregates were pelleted at 30000 xg for 20 min and 4°C. Cleared sample was loaded on a Superose 6 Increase 3.2/300 column equilibrated in buffer D, collecting elution fractions of 100 µL throughout the run. Peak fractions were right away used for cryo-grid preparation.

UV–visible difference spectroscopy

The sample obtained from the sucrose cushion step was analyzed for heme content and supercomplex composition using UV–visible difference spectroscopy and CN-PAGE combined with in-gel activity assays. UV–visible difference spectra were recorded between 390 and 675 nm using a home-built spectrophotometer. Protein samples were diluted as necessary in 50 mM

332 HEPES, 0.1% digitonin and pH 8.0. Spectra were measured from sodium dithionite-reduced
333 *minus* air-oxidized spectra. When multiple absorption bands overlapped, spectra were
334 deconvoluted using the peak analysis function in OriginPro 2015 (OriginLab Corporation,
335 Northampton, MA, USA).

336

337 Gel electrophoresis

338 NativePAGE™ 3 to 12%, Bis-Tris, 1.0 mm, Mini Protein Gel (Invitrogen) pre-cast gels were
339 used for Clear Native (CN) PAGE. The gels were loaded with a protein ladder (NativeMark™,
340 Invitrogen) and four identical sample lanes where the protein samples have been mixed with
341 NativePAGE™ Sample Buffer (final concentration, 50 mM BisTris, 6 N HCl, 50 mM NaCl,
342 10% w/v glycerol, 0.001% Ponceau S, pH 7.2) as per the manufacturer's instruction.
343 Electrophoresis was conducted at 4°C, first at 150 V for 30 min with NativePage Light Blue
344 Cathode buffer (50 mM BisTris, 50 mM Tricine, pH 6.8, 0.002% Coomassie G-250) and then at
345 250 V for 150 min with NativePAGE Anode Buffer (50 mM BisTris, 50 mM Tricine, pH 6.8).
346 In-gel activity assays were performed following published protocols[33]. In brief, each sample
347 lane from CN-PAGE was incubated with an aqueous solution to reveal (i) protein bands (0.02%
348 Coomassie G-250, overnight) or the presence of active (ii) CI (2 mM Tris pH 7.4, 2.5 mg/mL
349 nitrotetrazolium blue chloride (NBT), 0.1 mg/mL NADH, 15 min), (iii) CII (5 mM Tris pH 7.4,
350 2.5 mg/mL NBT, 84 mM succinic acid, 0.2 mM phenazine methosulfate, 30-40 min) and (iv)
351 CIV (0.05 mM KPi pH 7.4, 0.5 mg/mL 3,3′-diaminobenzidine (DAB), 1 mg/mL cytochrome *c*
352 from *Saccharomyces cerevisiae*, overnight). The reactions were stopped by incubation in 10 %
353 (v/v) acetic acid, followed by multiple exchanges of water. The gel shown is representative of
354 two experiments from two separate supercomplex preparations.

355

356 Cryo-EM sample preparation and data collection

357 Supercomplex eluted at a concentration of approximately 10 mg/mL. Aliquots of the peak
358 fraction were diluted in buffer D to 0.75 mg/mL before applied to cryo-grids. Quantifoil R2/2-
359 300 grids floated with a home-made 3 nm amorphous carbon layer were glow-discharged
360 immediately before applying a 3 uL sample. Grids were vitrified using liquid ethane cooled by
361 liquid nitrogen in a Vitrobot Mark IV, with 30 seconds wait time before blotting grids for 3
362 seconds at blot force 0. Micrographs were collected on a Titan Krios (ThermoFisher Scientific)
363 operated at 300 kV at a nominal magnification of 165 kx (0.83 Å/pixel) with a Quantum K2
364 camera (Gatan) using a slit width of 20 eV. With an objective lens aperture of 70 µm, images
365 were collected with an exposure rate of 4.26 electrons/pixel/second with 5 seconds exposure
366 fractionated into 20 frames. A total of 26,063 movies were collected.

367

368 Cryo-EM data processing

369 Motion correction was performed in the internal implementation of RELION-3.1[34], followed by
370 CTF estimation by CTFFIND 4. Initial rounds of particle picking and 2D classification, followed
371 by ab-initio reconstruction, 3D classification and preliminary refinement of the supercomplex.
372 Template-based particle picking in RELION was then used to pick and extract 1,664,103
373 particles. 2D classification and 3D heterogeneous refinement steps in cryoSPARC v.2[35] were
374 then used to separate supercomplex particles from copurified ATP synthase, resulting in a final
375 138,746 supercomplex particles used for subsequent refinement. Following a consensus
376 refinement in cryoSPARC, per-particle CTF refinement and bayesian polishing were performed
377 in RELION-3.1. For final refinements in cryoSPARC, particles were downsampled from a 724-
378 pixel box to 480 pixels, resulting in a pixel size of 1.25 Å/px. Masked refinements of the
379 respective supercomplex subregions resulted in map resolutions of 2.9 Å for the entire
380 supercomplex, 2.8 Å for complex-I, 3.0 Å for complex-II, 2.8 Å for complex-III and 2.6 Å for
381 complex-IV_2. Reported map resolutions are according to gold standard Fourier Shell Correlation
382 (FSC) using the 0.143-criterion. To assess flexibility of the Rieske subunit wedged in the CI-III_2
383 interface, we performed focused 3D-classification in RELION-3.1 using pre-aligned particles
384 with a mask on the extended area around the headgroup of the Rieske subunit. Classification into
385 10 classes resulted in maps confirming flexibility of the structural element, with two classes
386 corresponding closely to the previously reported b- and c-states (Fig. 3F and G).

387

388 Electron cryo-tomography and subtomogram averaging

389 Crude mitochondrial pellets were resuspended in an equal volume of buffer containing 20 mM
390 HEPES-KOH pH 7.4, 2 mM EDTA, 250 mM sucrose and mixed in a 1:1 ratio with 5-nm
391 colloidal gold solution (Sigma Aldrich) and vitrified as described above on glow-discharged
392 Quantifoil R2/2 Au 200 mesh grids. Tilt series were acquired on a Titan Krios operated at
393 300 kV with a K3 camera (slit width 20 eV) using serialEM or the EPU software (Thermo Fisher
394 Scientific). Mitochondrial membranes were imaged at a nominal magnification of 42 kx
395 (2.11 Å/pixel) and an exposure rate of 19.5 electrons/pixel/s with a 3 electron/$Å^2$ exposure per
396 tilt fractionated into five frames with tilt series acquired using the exposure-symmetric scheme[36]
397 to ±60° tilt and a 3° tilt increment. Following motion correction in motionCor2, tomographic
398 reconstruction from tilt series was performed in IMOD[37] using phaseflipping and a binning factor
399 2. Tomograms were contrast enhanced using nonlinear anisotropic diffusion filtering to facilitate
400 manual particle picking of supercomplex particles based on the matrix arm of complex-I.
401 Subtomogram averaging was performed in PEET[38]. Initial references were generated from the
402 data by averaging after rotating subvolumes into a common orientation with respect to the
403 membrane based on manually assigned vectors. Following initial rounds of averaging to generate
404 a suitable reference, data was manually split into half-sets and refined independently, following
405 lowpass filtering to 50 Å. Averaging of 360 particles from 12 tomograms resulted in a 28-Å
406 subtomogram average.

407

408 Model building and refinement

409 Manual model building was performed in *Coot*[39], and new subunits identified directly for the
410 cryo-EM map. For identified canonical subunits, homology models were generated using SWISS
411 modeler. Bound cardiolipins were unambiguously identified from their head group density.
412 Other natively bound lipids were tentatively modelled as phosphatidylcholine,
413 phosphatidylethanolamine or phosphatidic acid based on head group densities. Real-space
414 refinement of atomic models was performed in PHENIX using secondary structure restraints[40].
415 Atomic model statistics were calculated using MolProbity[41].

416 Given the mild solubilization conditions we used, for $CIII_2$ cryo-EM map showed density located
417 on the pseudo-C_2 symmetry axis between the two COB heme b_L molecules displaying planar
418 map features consistent with the quinone moiety of ubiquinone (UQ). Interestingly, the density
419 clearly indicates that UQ can bind in two orientations, related by the symmetry rotation of the
420 dimer. In either of the two orientations, the quinone moiety is positioned close to a heme b_L,
421 where potentially it could accept electrons for transfer across the dimer axis. In the recent
422 amphipol $CIII_2$ structure[7], the isoprenoid tail of UQ was modeled in the equivalent position,
423 however, planar density for the quinone was missing. This orientation-equivalent binding of UQ
424 between the two COB heme b_L molecules, together with the B- and C-state Rieske
425 conformations, suggest a maintained functional symmetry of ciliate $CIII_2$ within the
426 supercomplex.

427 In the CI, we identified 49 canonical subunits and 21 subunits that we assign as phylum-specific.
428 In each CIV monomer, we identified 11 subunits homologous to mammalian CIV (COX1, 2, 3a,
429 3b, 5B, 6A, 6B, 6C, 7A, 7C, NDUFA4) and 42 ciliate-specific subunits, most of which are
430 peripherally associated around the mitochondrial protein core. Three of the mammalian subunits
431 missing in *T. thermophila* CIV (COX4, COX7B, and COX8) are at the interface where two
432 mitochondrial carriers are bound. The mitochondrially encoded core subunit COX3 is split into
433 two fragments. Most of the TM helices are contributed by the C-terminal COX3b, which is
434 encoded by the mitochondrial *ymf68* gene. The newly annotated Ymf68 is structurally conserved,
435 apart from the missing helix (H1), which is structurally replaced by Ymf67. We therefore assign
436 *ymf67* and *ymf68* of the ciliate mitochondrial genome as separately encoding the COX3a/b
437 subunit fragments. On the *T. tetrahymena* mitochondrial genome, *ymf67* and *ymf68* genes are
438 located on the same strand, but separated by the gene for tRNATrp, suggesting that a
439 transposition event may have led to the fragmentation of the original COX3 gene. tRNA genes
440 are known to be among the most motile elements in metazoan mtDNA. Both COX3a/b
441 fragments have evolved substantial subunit extensions threading through the augmented CIV
442 monomer unit to recruit lineage-specific subunits and mediate supercomplex assembly.
443 In the CIV dimer, the dimer interface of 17,000-$Å^2$ is dominated by 16 species-specific subunits.
444 Furthermore, when aligned on the CIV core, a comparison of the mammalian and ciliate
445 structures reveals that the two dimers display markedly different architectures, dimer axes and
446 distances between COX1 cores. This suggests that the ciliate CIV dimerization likely evolved

447 through the acquisition of lineage-specific subunits and reflects the constraints of the unique
448 tubular membrane environment.
449 In addition, each CIV monomer complex contains two different Surf1-like proteins, which in
450 human were reported to complement defects causing the Leigh syndrome. In our structure, two
451 Surf1-like proteins are permanently attached to CIV and display similar overall structures,
452 consisting of a lumen-exposed soluble domain and a transmembrane-helix hairpin. The two
453 Surf1 proteins are facing each other, bound on opposite sides of each CIV core.
454 The presence of subunit extension and accessory subunits in CIV generates a pronounced cavity
455 around the cytochrome *c* binding site. However, overlaying of a *Tetrahymena* cytochrome *c*
456 homology model suggests that the canonical binding site is not obstructed. Cytochrome *c* binding
457 is known to be driven by electrostatic interactions with the CuA domain of COX2, which in
458 mammals forms a negatively charged patch. This structural feature is positively charged in *T.*
459 *thermophila*, interacting mainly with H1 of cytochrome *c*, which displays a flipped polarity. We
460 conclude that the experimentally observed functional incompatibility of *Tetrahymena* CIV and
461 mammalian cytochrome *c* is not due to divergent architecture, but an inverted surface charge of
462 the binding pocket.
463

464 Molecular dynamics simulations

465 We performed coarse-grained (CG) molecular dynamics (MD) simulations on the entire
466 *Tetrahymena thermophila* supercomplex structure using Martini3 forcefield[42] to study the
467 rearrangement of the lipid bilayer around the highly bent protein assembly. Using the *martinize2*
468 (version 2.6) tool, we transformed the atomistic structure into a CG model (atoms clustered into
469 Martini beads)[43]. Using the small molecules database and the existing topologies of
470 phospholipids available in the Martini3[42] forcefield, we generated the force field parameters for
471 cardiolipin. Cofactors and resolved lipids in the structure were not included in the simulated
472 model system, and only protein was simulated to study the dynamics of lipid molecules around
473 it. First, the CG model of the protein structure was minimized for 100 steps in vacuum to remove
474 possible steric clashes. Then the minimized CG supercomplex was embedded in a large (75 nm x
475 75 nm) hybrid membrane slab (POPE:POPC:CL in 4:2:1 ratio) using the *insane.py* script[44]. The
476 coarse-grained protein-membrane system was solvated using standard Martini3 water beads and
477 100 mM Na^+ and Cl^- ions. Starting from this initial position, the simulation system was
478 minimized keeping all beads free; first in double precision to resolve steric clashes between the
479 lipids (maximum 500 steps) and then in regular single precision (maximum 10 000 steps). After
480 minimization, with 4000 kJ mol^{-1} nm^{-2} harmonic constraints on the backbone beads, the system
481 was equilibrated using velocity-rescaling thermostat[45] and Berendsen barostat[46] for 10
482 nanoseconds. During production runs, the 4000 kJ $mol^{-1}nm^{-2}$ harmonic constraints on the
483 backbone beads were applied. Velocity-rescaling thermostat[45] and Parrinello-Rahman barostat[47]
484 were used for temperature (310 K) and pressure (1 bar) control in the production phase.
485 Coulombic interactions were treated with the reaction-field algorithm using $\varepsilon_r = 15$[48]. The Verlet
486 cutoff scheme was implemented with a Lennard-Jones cutoff of 1.1 nm[49]. The time step of the

487 coarse-grained MD simulations was 20 femtoseconds. Initial simulation replicas showed
488 incomplete or unstable wrapping of the membrane around the protein, so we translated the lipid
489 bilayer patch in z-direction and altered the insertion angle of the supercomplex to find an initial
490 position that allowed the membrane to equilibrate and wrap fully around the protein (Systems
491 T1-T7, simulation lengths 0.9 – 2.8 µicroseconds, total 9.6 µicroseconds). After finding the
492 correct insertion of the protein into the membrane, we initiated three independent simulation
493 replicas (Systems P1-P3, simulation lengths 10 µicroseconds each, total 30 µicroseconds). The
494 simulations were performed using the Gromacs software (version 2021)[50].

495

496 Data visualization and analysis

497 Images were rendered using ChimeraX[51]. To analyze the *T. thermophila* cytochrome-c binding
498 site, the mammalian cytochrome-c bound complex-IV structure (PDB 5iy5) was overlaid with
499 the *T. thermophila* structure. Using AlphaFold2[52], a *T. thermophila* cytochrome-c structure was
500 predicted and overlaid into both the mammalian structure and *T. thermophila* structures. The
501 composite map of the complete respiratory supercomplex was generated in ChimeraX. This map
502 was only used for visualization, but not for atomic model refinement, where instead a consensus
503 map was used. The buried areas of the CI-CII-$CIII_2$-CIV_2 interfaces and CIV dimer interface was
504 calculated in ChimeraX[51].

505

506 **Data availability statement**

507 The atomic coordinates were deposited in the RCSB Protein Data Bank (PDB) under accession
508 number XXXX. The cryo-EM maps have been deposited in the Electron Microscopy Data Bank
509 (EMDB) under accession number EMD-XXXXX.

510

511 **Additional References**

512 33. P. Jha, X. Wang, J. Auwerx, Analysis of Mitochondrial Respiratory Chain Supercomplexes
513 Using Blue Native Polyacrylamide Gel Electrophoresis (BN-PAGE). *Curr Protoc Mouse*
514 *Biol* **6**, 1-14 (2016).

515 34. J. Zivanov *et al.*, New tools for automated high-resolution cryo-EM structure determination
516 in RELION-3. *eLife* **7**, (2018).

517 35. A. Punjani, J. L. Rubinstein, D. J. Fleet, M. A. Brubaker, cryoSPARC: algorithms for rapid
518 unsupervised cryo-EM structure determination. *Nat Methods* **14**, 290-296 (2017).

519 36. W. J. H. Hagen, W. Wan, J. A. G. Briggs, Implementation of a cryo-electron tomography
520 tilt-scheme optimized for high resolution subtomogram averaging. *J Struct Biol* **197**, 191-
521 198 (2017).

522 37. J. R. Kremer, D. N. Mastronarde, J. R. McIntosh, Computer visualization of three-
523 dimensional image data using IMOD. *J Struct Biol* **116**, 71-76 (1996).

38. D. Nicastro *et al.*, The molecular architecture of axonemes revealed by cryoelectron tomography. *Science* **313**, 944-948 (2006).

39. P. Emsley, K. Cowtan, Coot: model-building tools for molecular graphics. *Acta Crystallogr D Biol Crystallogr* **60**, 2126-2132 (2004).

40. P. V. Afonine *et al.*, Real-space refinement in PHENIX for cryo-EM and crystallography. *Acta Crystallogr D Struct Biol* **74**, 531-544 (2018).

41. V. B. Chen *et al.*, MolProbity: all-atom structure validation for macromolecular crystallography. *Acta Crystallogr D Biol Crystallogr* **66**, 12-21 (2010).

42. P. C. T. Souza *et al.*, Martini 3: a general purpose force field for coarse-grained molecular dynamics. *Nat Methods* **18**, 382-388 (2021).

43. D. H. de Jong *et al.*, Improved Parameters for the Martini Coarse-Grained Protein Force Field. *J Chem Theory Comput* **9**, 687-697 (2013).

44. T. A. Wassenaar, H. I. Ingolfsson, R. A. Bockmann, D. P. Tieleman, S. J. Marrink, Computational Lipidomics with insane: A Versatile Tool for Generating Custom Membranes for Molecular Simulations. *J Chem Theory Comput* **11**, 2144-2155 (2015).

45. G. Bussi, D. Donadio, M. Parrinello, Canonical sampling through velocity rescaling. *J Chem Phys* **126**, 014101 (2007).

46. H. J. C. Berendsen, J. P. M. Postma, W. F. Vangunsteren, A. Dinola, J. R. Haak, Molecular-Dynamics with Coupling to an External Bath. *Journal of Chemical Physics* **81**, 3684-3690 (1984).

47. M. Parrinello, A. Rahman, Polymorphic Transitions in Single-Crystals - a New Molecular-Dynamics Method. *J Appl Phys* **52**, 7182-7190 (1981).

48. I. G. Tironi, R. Sperb, P. E. Smith, W. F. Vangunsteren, A Generalized Reaction Field Method for Molecular-Dynamics Simulations. *Journal of Chemical Physics* **102**, 5451-5459 (1995).

49. H. Grubmuller, H. Heller, A. Windemuth, K. Schulten, Generalized Verlet Algorithm for Efficient Molecular Dynamics Simulations with Long-Range Interactions. *Molecular Simulation* **6**, 121-142 (1991).

50. M. J. Abraham *et al.*, GROMACS: High performance molecular simulations through multi-level parallelism from laptops to supercomputers. *SoftwareX* **1-2**, 19-25 (2015).

51. T. D. Goddard *et al.*, UCSF ChimeraX: Meeting modern challenges in visualization and analysis. *Protein Sci* **27**, 14-25 (2018).

52. J. Jumper *et al.*, Highly accurate protein structure prediction with AlphaFold. *Nature* **596**, 583-589 (2021).

Acknowledgments

We thank SciLifeLab EM facility (funded by the KAW, EPS, and Kempe foundations), EMBO Young Investigator Program, Biological Physics group at the University of Helsinki and Dr. Paulo C. T. Souza for discussions on MD simulations; Swedish Foundation for Strategic Research (FFL15:0325), Ragnar Söderberg Foundation (M44/16), Cancerfonden (2017/1041), European Research Council (ERC-2018-StG-805230), Knut and Alice Wallenberg Foundation (2018.0080), V.S. was supported by Academy of Finland, Sigrid Jusélius Foundation, Jane and Aatos Erkko Foundation, Magnus Ehrnrooth Foundation and the University of Helsinki, A. Ma. was supported by Medical Research Council (CDA MR/M00936X/1, Transition Support MR/T032154/1).

Author contributions

A.M., R.K.F. and A.A. designed the project. V.T. performed cell culturing and isolation of mitochondria. A.M. and R.K.F. prepared the sample and collected cryo-EM data. A.M., R.K.F. and R.B. processed cryo-EM data and built the model. A.M. performed cryo-ET and subtomogram averaging. O.H. and V.S. performed molecular dynamics simulations. T.G, A.Ma., and A.A. performed biochemical and spectroscopic analyses. A.M., R.K.F. and A.A. wrote the manuscript with contributions from O.H., V.S and A.Ma. All authors contributed to revising the manuscript.

Competing interests

Authors declare no competing interests.

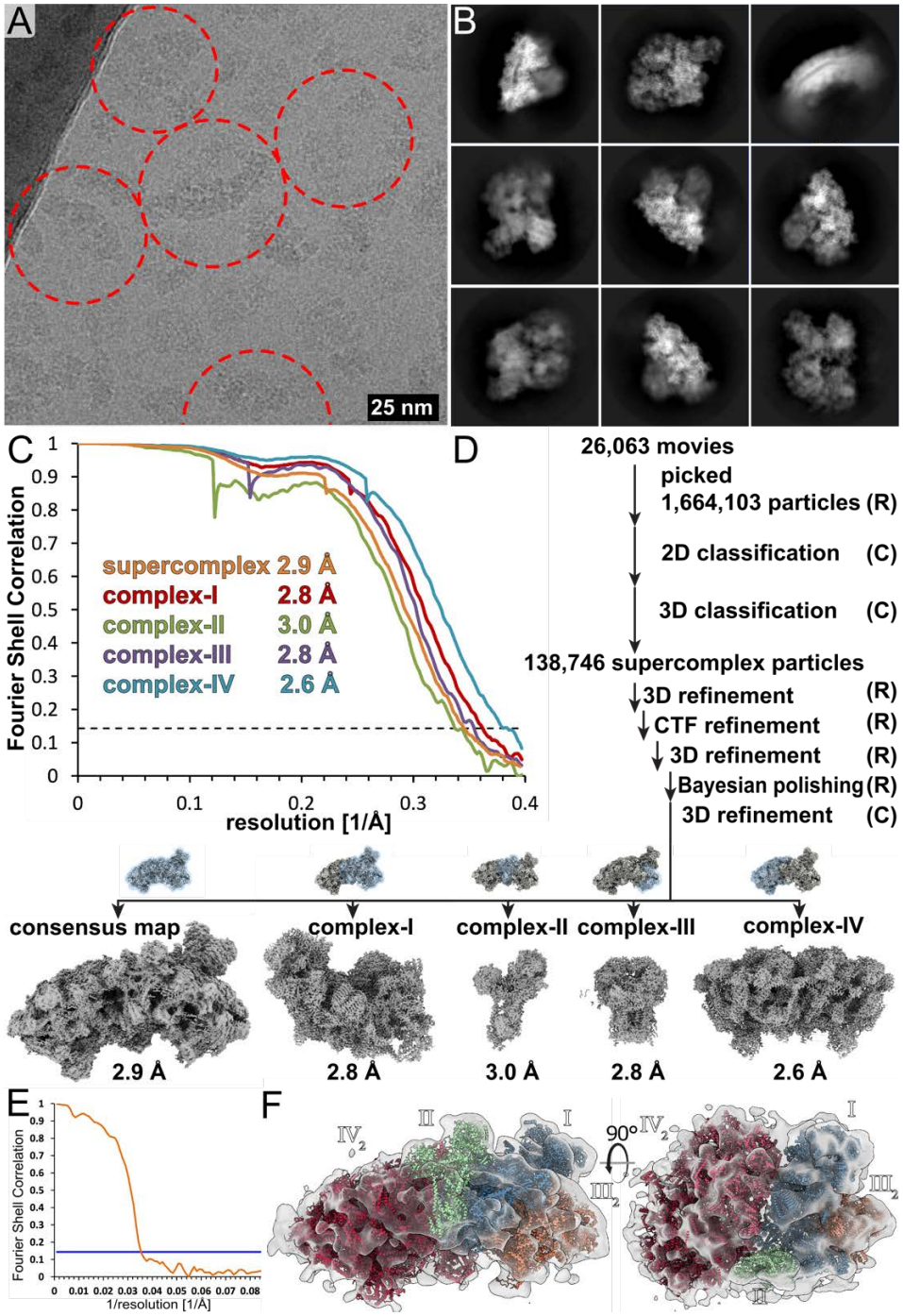

Extended Data Fig. 1. Cryo-EM and subtomogram averaging data processing. (A) representative micrograph with supercomplex particles indicated. **(B)** 2D class averages. **(C)** Fourier Shell Correlation of the five final maps according to the 0.143 gold-standard criterion. **(D)** particle processing workflow in RELION-3.1 (R) and cryoSPARC2 (C). **(E)** Fourier Shell correlation of the subtomogram average indicating a resolution of 28 Å. **(F)** The subtomogram average map (transparent grey) agrees well with the atomic model of the I-II-III_2-IV_2.

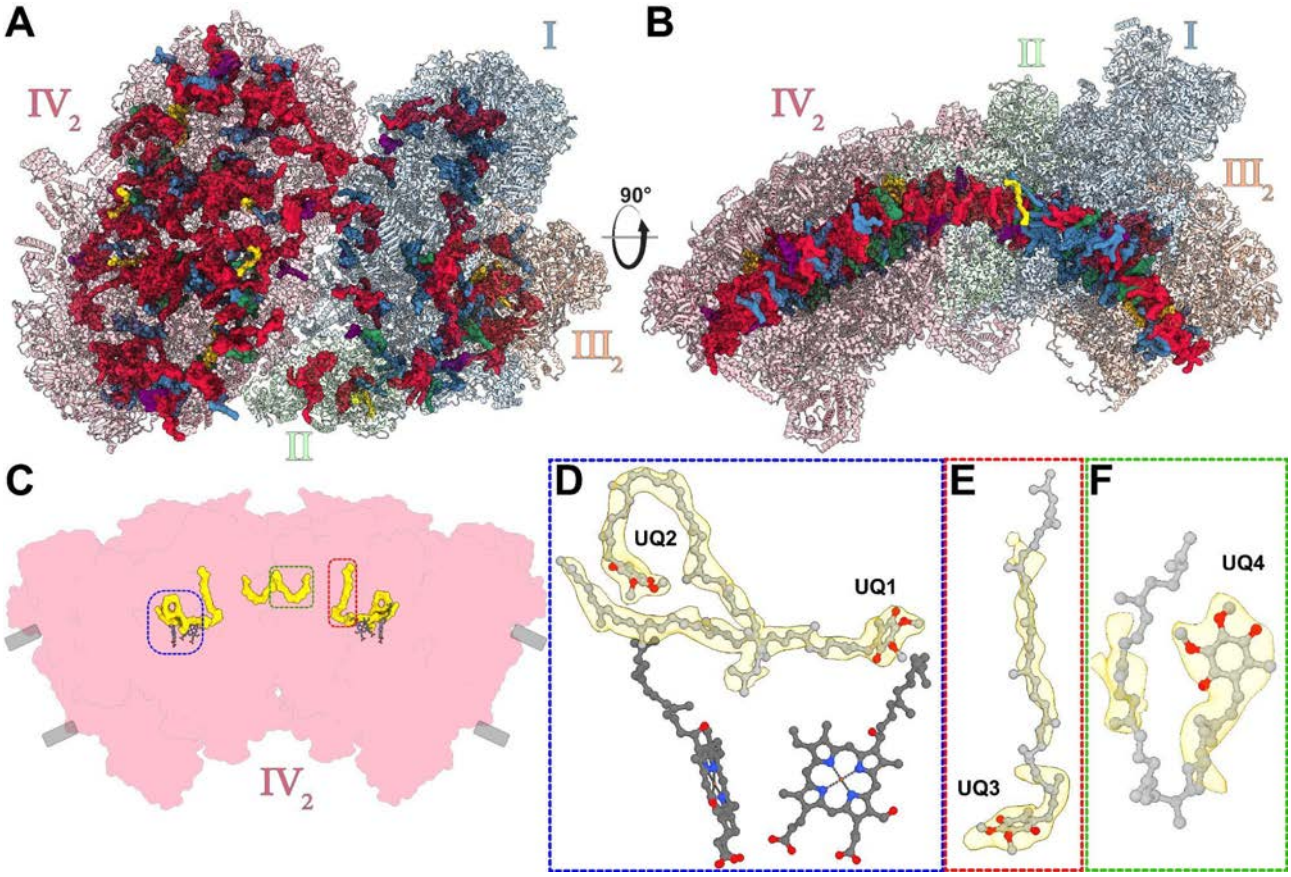

Extended Data Fig. 2. Bound native lipids of the ciliate I-II-III$_2$-IV$_2$ supercomplex reveal a curved membrane region. Top view **(A)** and side view **(B)** of the supercomplex structure with bound lipids cardiolipin (red), phosphatidylcholine (blue) phosphatidylethanolamine (green), phosphatidic acid (yellow), phosphatidic acid (yellow), ubiquinone-8 (purple) spread throughout the membrane region. **(C-F)** Location of the four ubiquinone-8 molecules found in each CIV monomer with closeup views **(D-F)**, including two UQ-8 molecules bound close to the heme centres **(D)**.

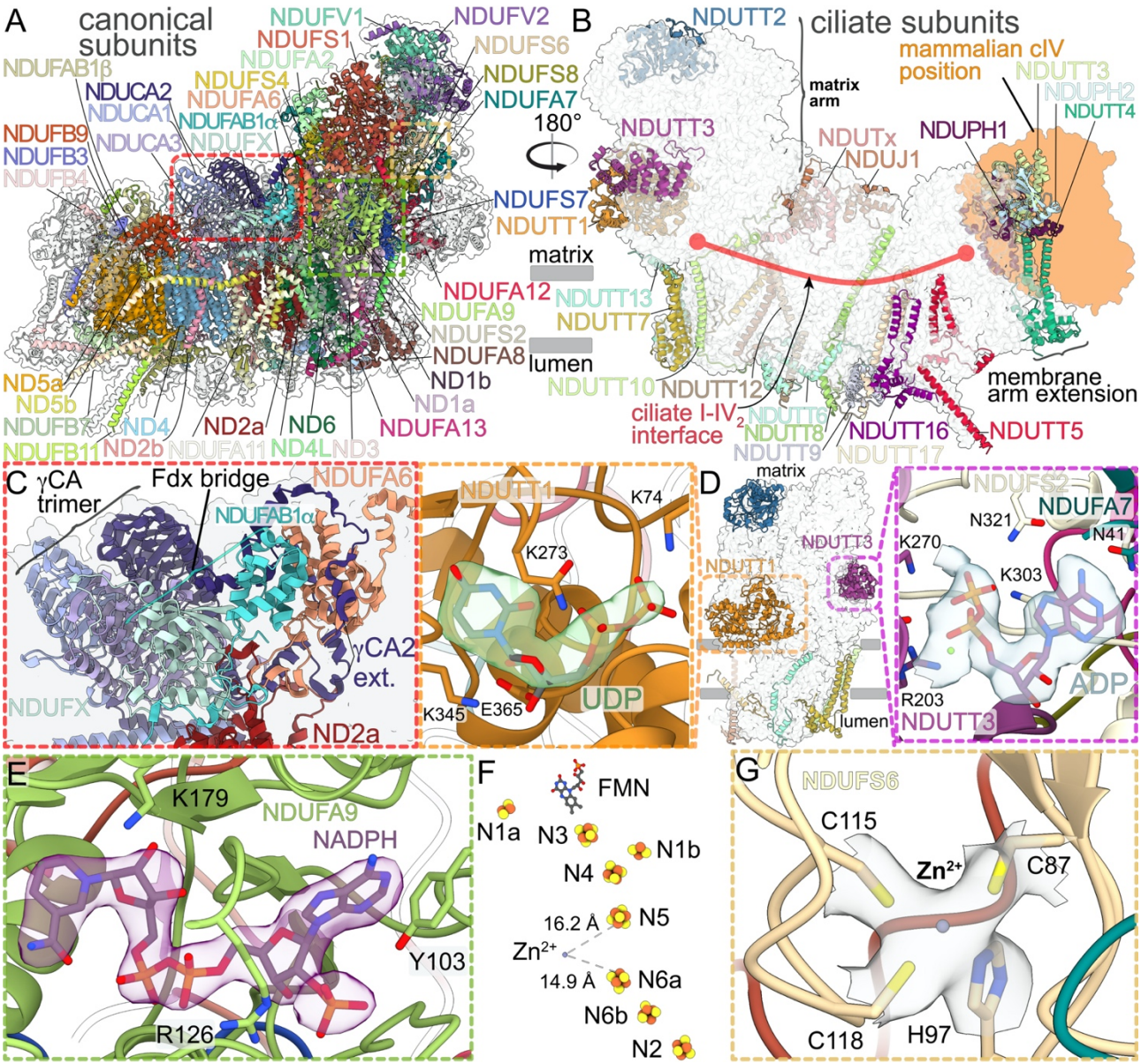

Extended Data Fig. 3. Lineage-specific structural features of CI dictate a divergent supercomplex architecture. The canonical subunits of CI (coloured) include the conserved antiporter-like folds (ND2a/b, ND4, ND5a/b), as well as a γ-carbonic anhydrase trimer. **(B)** The augmented CI architecture occludes the canonical CIV binding site. **(C)** The ferrodoxin bridge of NDUAB1-a and NDUFX connects ND2a of the membrane arm and NDUA6 of the matrix arm. **(D)** The matrix arm contains bound soluble subunits NDUTT1 with a bound UDP and NDUTT3 with a bonus ADP. **(E)** NDUFA9 contains a bound NADPH molecule located close to the CI Q-tunnel. **(F)** Overview of redox active centers in CI matrix arm including the **(G)** zinc ion coordinated by three Cys and one His residue within NDUS6.

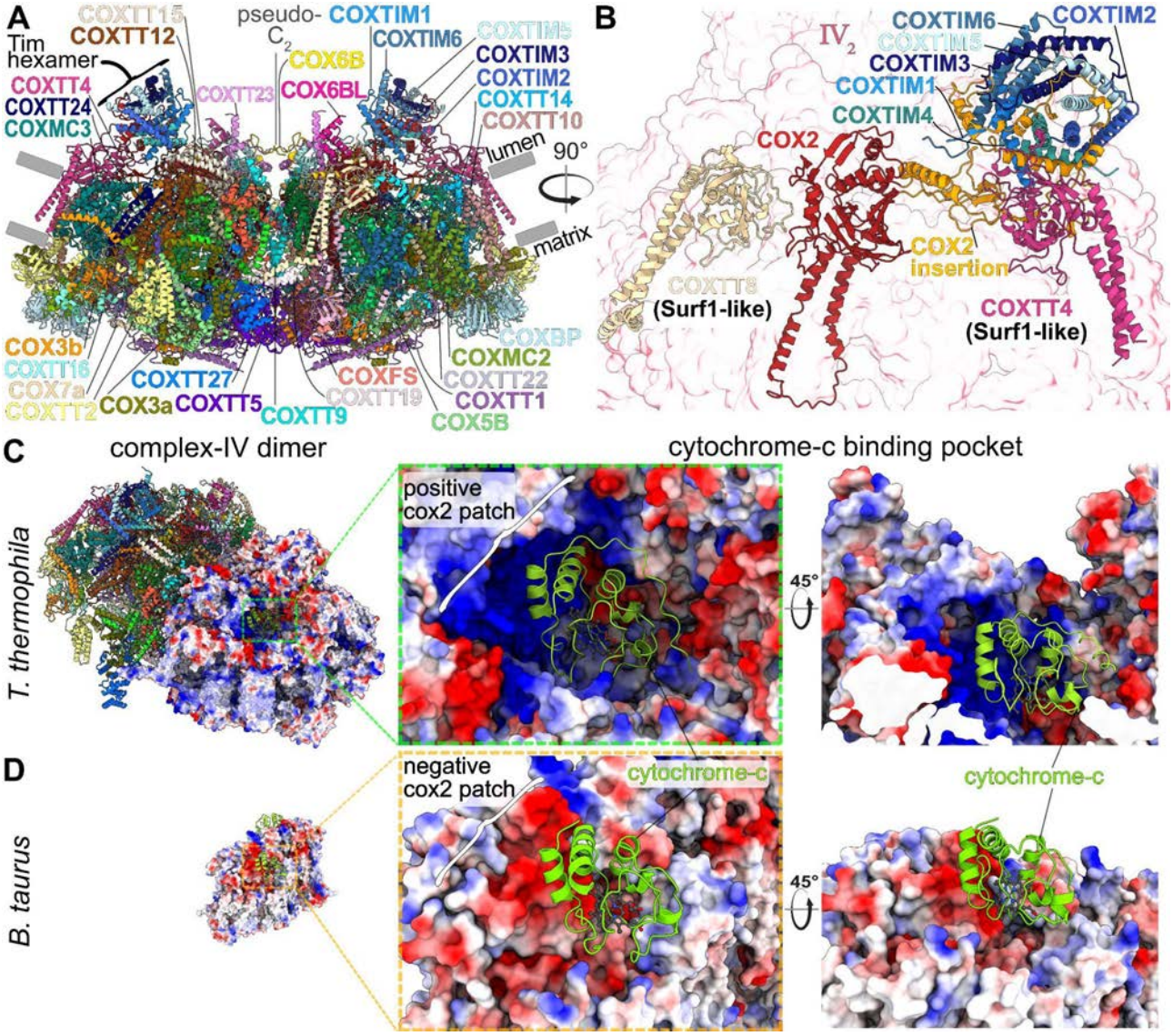

Extended Data Fig. 4. CIV_2 contains a bound Tim hexamer and a cytochrome-*c* binding site with inverted electrostatic charge. (A) sideview of CIV_2, containing numerous accessory subunits, including a Tim hexamer (B) Closeup view of COX2, which contains an insertion that recruits the Tim hexamer to the CIV dimer. Furthermore, COX2 interacts with the two Surf1-like proteins COXTT8 and COXTT4. **(C-D)** ciliate (C, this study) and mammalian (D, PDB 5IY5) CIV_2 structures. An overlay of a predicted Tt-cytochrome-c structure fits the cytochrome-c binding crater without clashes, suggesting that the difference in binding affinities is derived from inverted surface charge of the COX2 patch on the binding site.

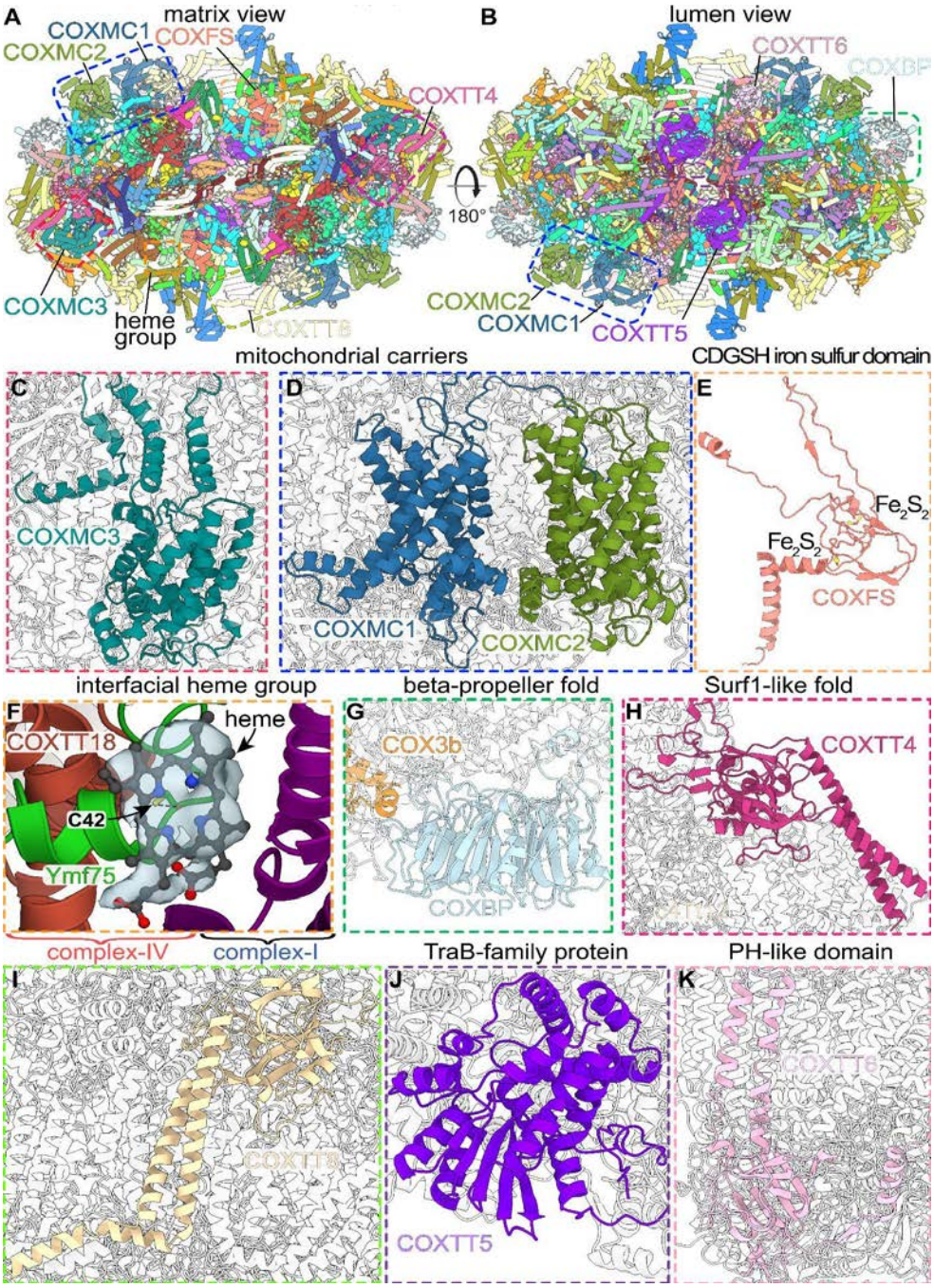

Extended Data Fig. 5. The augmented CIV dimer contains numerous associated compact-fold subunits. (A,B) Matrix and lumen view of the CIV dimer, subunit locations of insets are indicated. (**C,D**) Subunits COXMC1,MC2 and MC3 form mitochondrial carrier folds. COXFS is a CDGSH iron sulfur domain **(E).** A similar recruitment of a CDGSH-like protein has been found in the *T. thermophila* mitochondrial ribosome, where mL107 plays a structural role in the large mitochondrial subunit (Tobiasson et al). **(F)** Ymf75 coordinates a noncanonical heme group at the CIV periphery. (**G-K**) Compact folds of accessory subunits include a seven-bladed beta-propeller (G), two Surf1-like proteins (H, I) a TraB-family protein (J) and a Pleckstrin homology (PH) like domain (K).

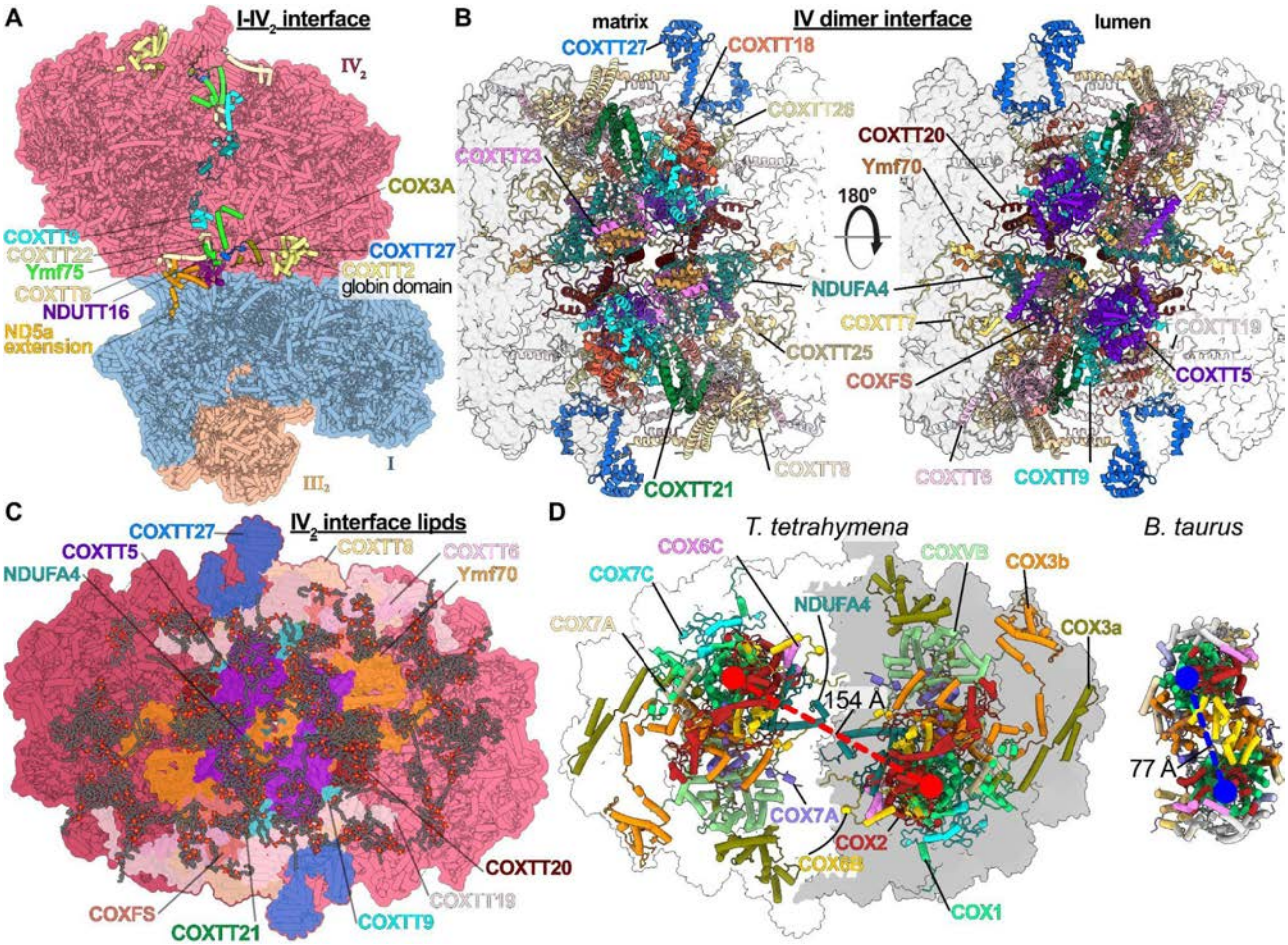

Extended Data Fig. 6. Formation of an augmented CIV dimer enables divergent supercomplex assembly. (A) The I-II-III2-IV2 supercomplex displays additional subunits and ordered structural elements (colored cartoons) compared to the amphipol embedded, isolated CIV_2 dimer (PDB 7W5Z). Additional features of the CI-IV interface include subunit NDUTT16 as well as an entire globin-like domain of COXTT2. **(B)** Matrix and lumenal views of the CIV_2 interface include NDUFA4. **(C)** The CIV_2 contains 210 lipids, many of which populate the dimer interface region. **(D)** The *T. thermophila* dimer is augmented compared to the bovine dimer structure and contains the previously unassigned canonical subunit NDUFA4, which is absent in the bovine dimer (right, PDB 3X2Q). Vectors (red, blue) indicate different distances between COX1 centers.

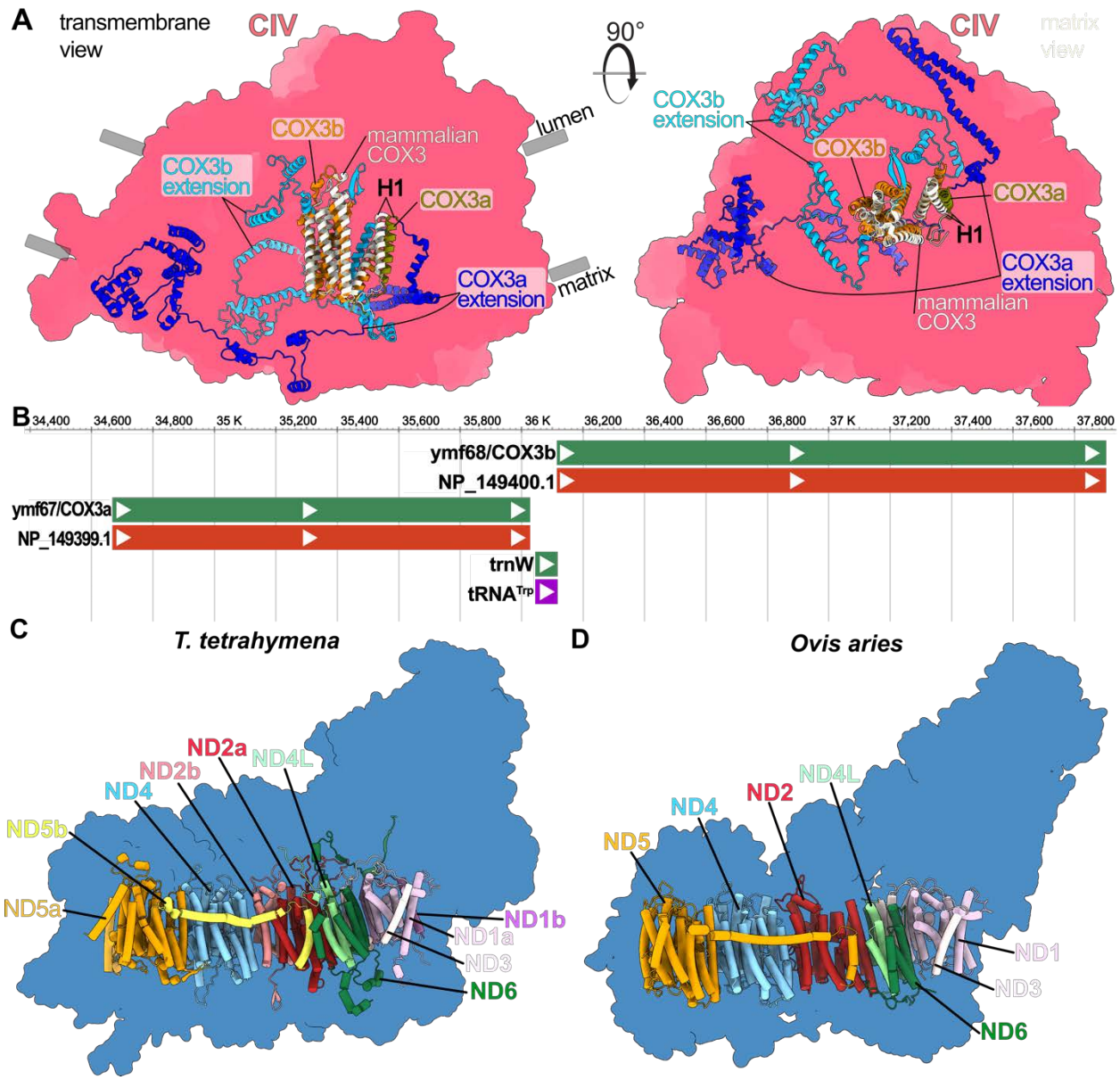

Extended Data Fig. 7. Fragmentation and extension of COX3 and CI proton-pump subunits. (A) Overlay of the mammalian COX3 (PDB 5IY5) and the Tt-COX3 (this study) shows that the N-terminal fragment (COX3a), encoded by *ymf67* corresponds to Helix-1 (H1) of the conserved structure. COX3b, encoded by *ymf68* makes up most of the conserved COX3 fold and contains large extensions that contribute to accessory subunit recruitment and supercomplex formation. **(B)** *T. thermophila* mitochondrial genome region showing the insertion of the tRNA-Trp gene in between *ymf67*/COX3a and *ymf68*/COX3b (genes in green, protein/RNA transcripts in red and purple). **(C)** ciliate CI outline (blue) with the antiporter-like subunits shown in color-coded ribbons. The canonical proton pumps ND1, ND2 and ND5 are encoded by split genes, thus resulting in chimeric proteins with a and b chains. **(D)** mammalian CI outline (blue, PDB 5LNK) with subunits shown in ribbons color-coded as in A, showing the single-chain ND1-6 proteins.

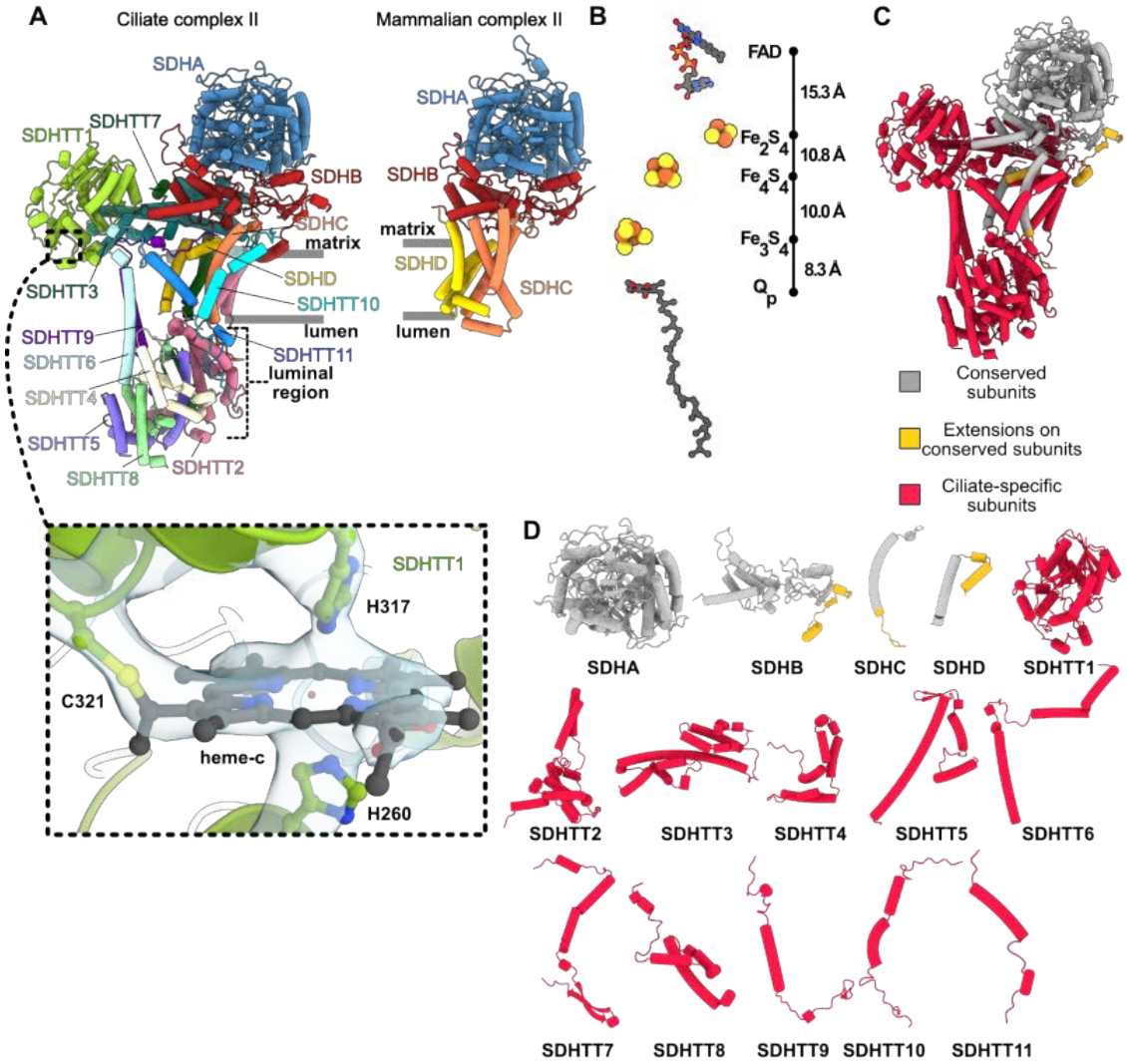

Extended Data Fig. 8. Conservation and divergence of ciliate CII. (A) Ciliate CII (left) colored by subunits and shown in comparison to mammalian CII (right, PDB 1ZOY) with similar color scheme for subunits SDHA-D. Evidently, the ciliate SDHC and SDHD subunits are substantially reduced in size and replaced by ciliate-specific subunits. Ciliate CII contains a sizable luminal protein region, whereas mammalian CII contains no equivalent region. Dashed window on SDHTT1 marks the view of a noncanonical cysteine-linked heme C that is coordinated by two axial histidines in SDHTT1E. **(B)** Conserved electron transfer chain in CII. **(C)** CII colored by conserved subunits (grey), extensions to conserved subunits (gold) and ciliate-specific subunits (red). Conservation is assessed as structural homology to mammalian CII (PDB 1ZOY). The ciliate CII shows a high degree of conservation for the four core SDHA-D subunits, with the ciliate-specific subunits essentially making up all the luminal domains, half of the transmembrane domains and half of the matrix domains. **(D)** Individual CII subunits shown as gallery with similar color coding as in C. Subunit naming follows the scheme in (*7*) with SDHTT1 being of largest Mw and SDHTT11 of the smallest molecular weight.

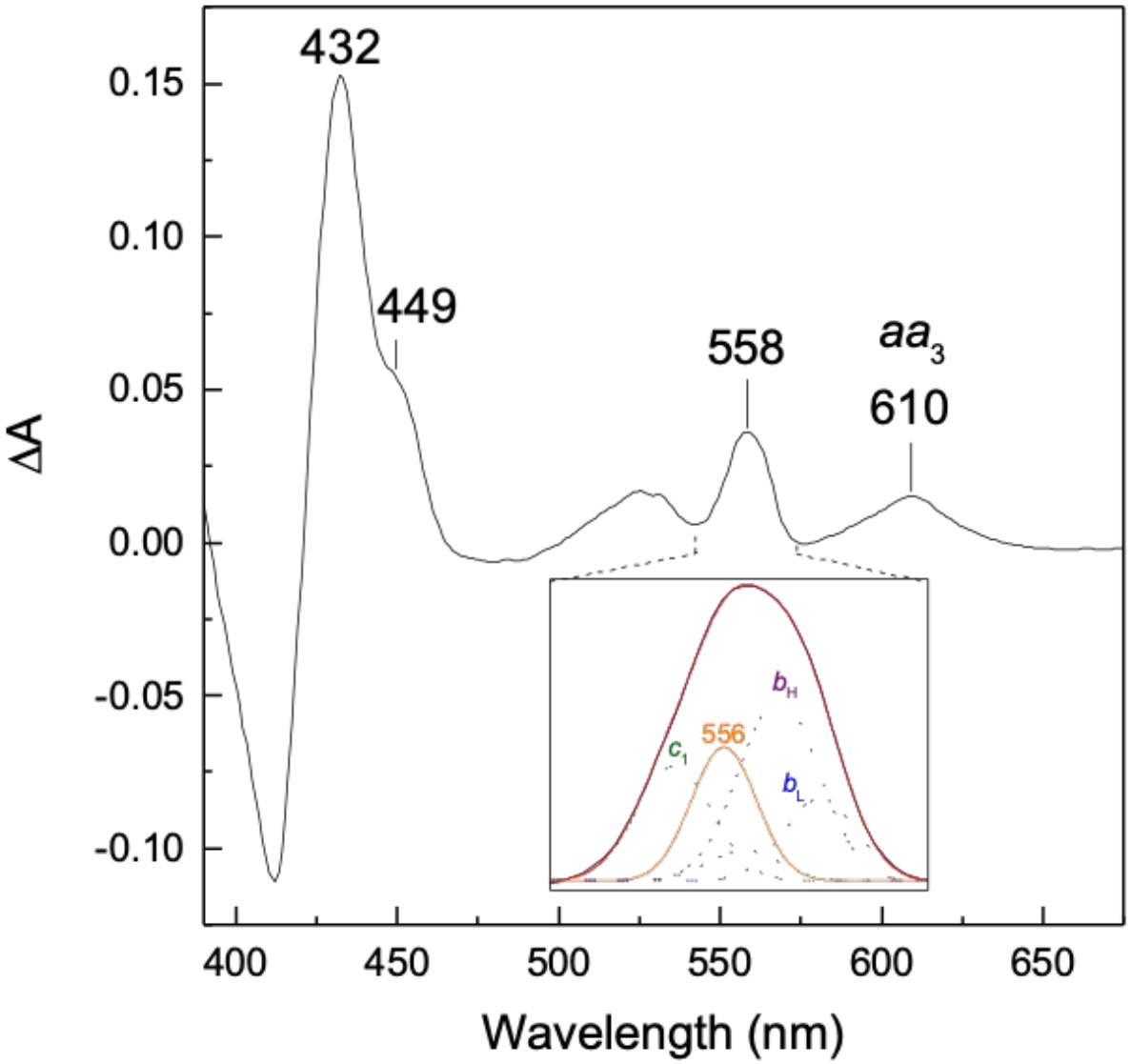

Extended Data Fig. 9. UV-visible redox absorption spectrum of the supercomplex. The dithionite minus air-oxidized difference spectrum was recorded in a 0.3 cm quartz cuvette after twofold dilution of the final sample in 50 mM HEPES, 0.1% digitonin, pH 8.0. Peaks are labeled that correspond to the absorption of the A-type hemes present in CIV (449/610 nm, aa_3) as well as merged absorption bands of other B- and C-type hemes (maxima at 432/558 nm). Inset: Deconvolution of the 558-nm absorption band to highlight the contribution of the B- and C-type hemes of CIII (b_H at 561 nm, purple; b_L at 558 and 565 nm, blue; c_1 at 552 nm, green) and the presence of at least another heme-protein with absorption maximum at 556 nm (orange). The spectrum shown is representative of two separate supercomplex preparations.

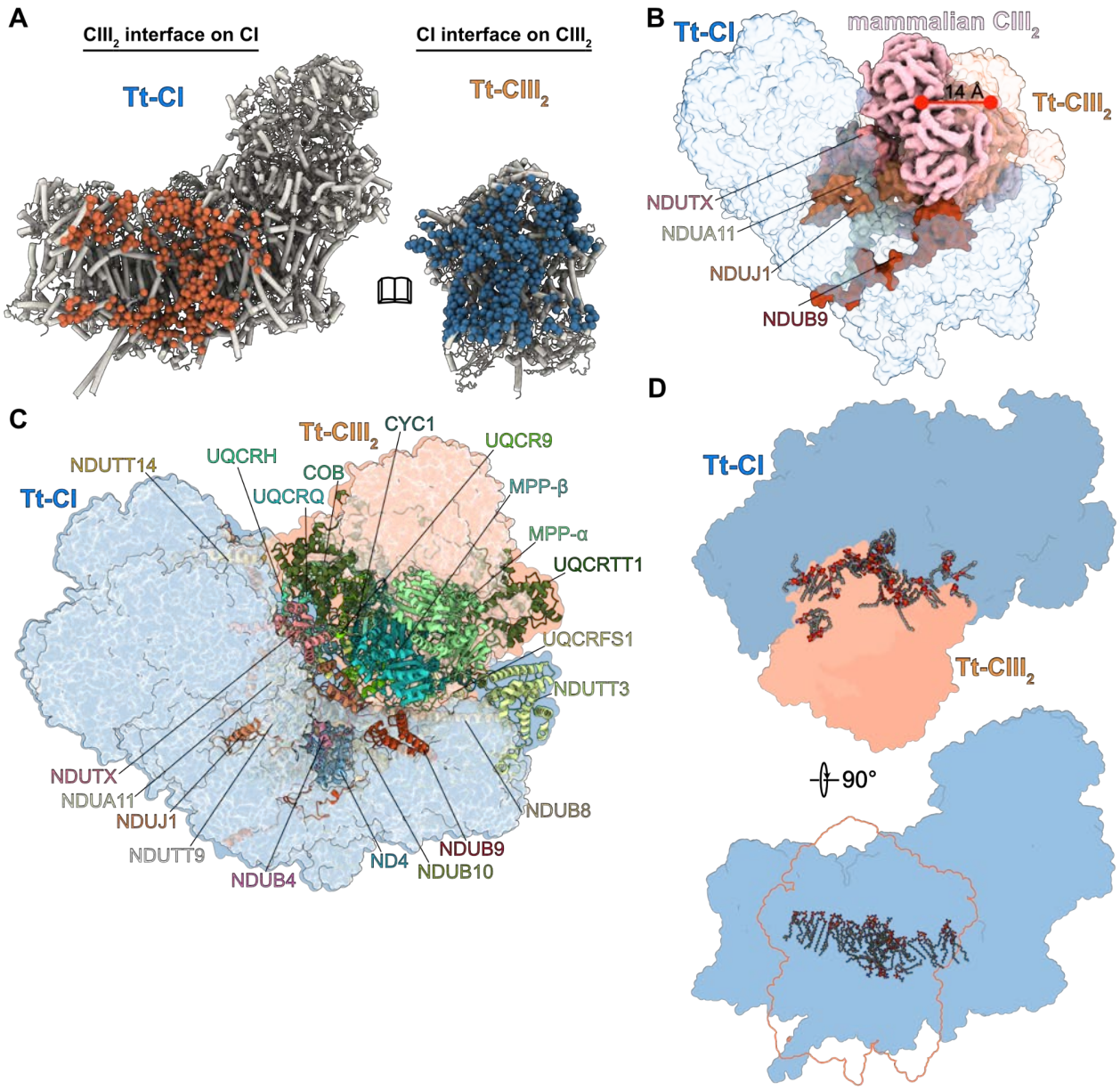

Extended Data Fig. 10. CI-CIII$_2$ interface is extensive and involves numerous lipids. (A) Buried surfaces in the CI-CIII$_2$ interface. Orange spheres show CIII$_2$ contacts on CI, blue spheres show CI contact points on CIII$_2$. Both sides of the CIII dimer interact with CI resulting in a >9,000 Å^2 interface. **(B)** Matrix view shows that four Tt-CI subunits would clash with mammalian CIII$_2$ in canonical position, thus Tt-CIII$_2$ is displaced 14 Å from Tt-CI. **(C)** CI outline (light blue surface) and CIII$_2$ outline (light orange surface) highlights the docked position of CIII$_2$ on the concave side of the bent CI membrane arm. All subunits that participate in CI-CIII$_2$ interface interactions are shown in ribbons and colored as in Fig. 2A,B and Fig. S6A. Non-interacting subunits of CI and CIII$_2$ are shown in transparent, light grey surface. **(D)** Orthogonal views of bound native lipids in the I-III$_2$ interface. Lipids are distributed in both matrix and luminal leaflets.

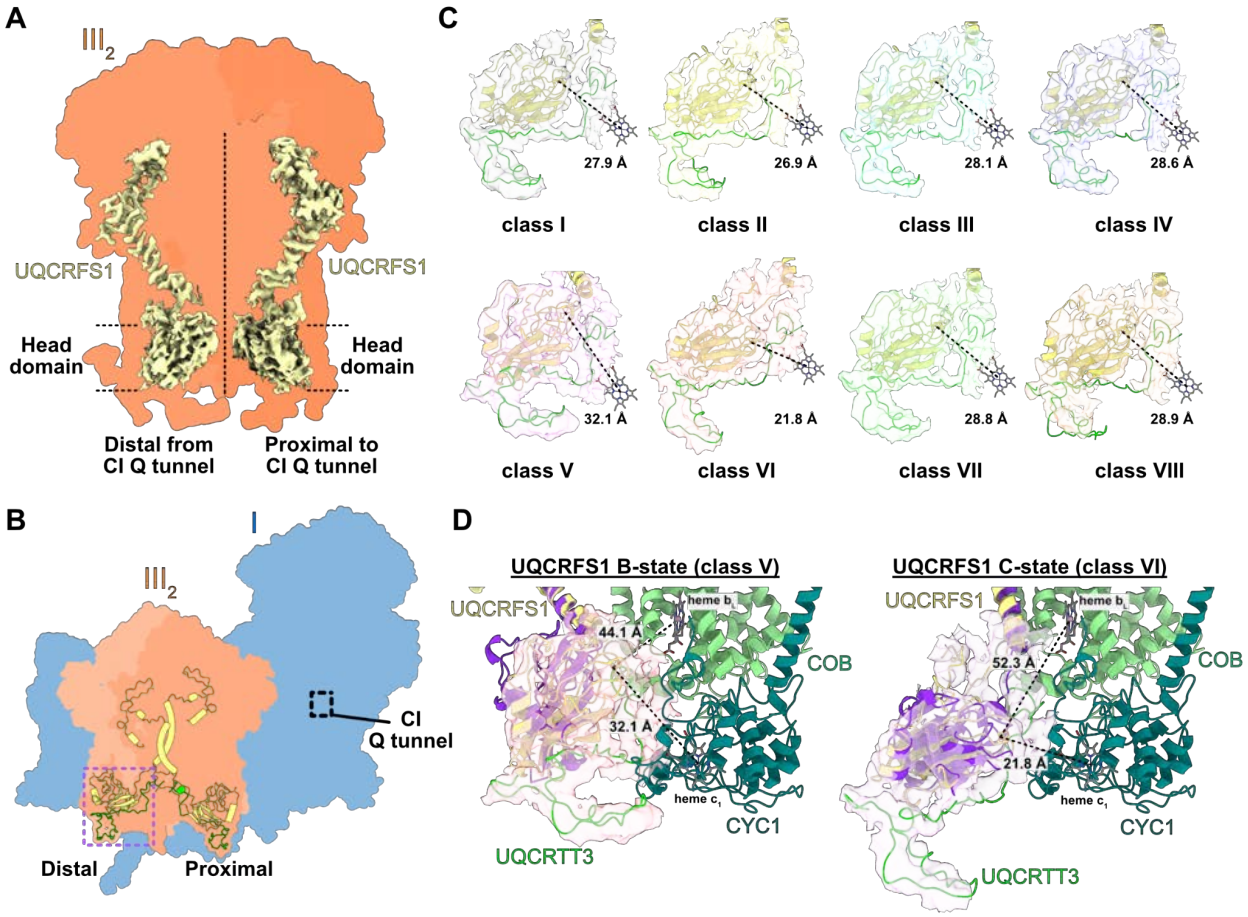

Extended Data Fig. 11. Conformational flexibility in distal UQCRFS1 head domain. (A) cryo-EM map density carved around the UQCRFS1 proteins in $CIII_2$. Head domain map density for both copies show similar features of inherent flexibility. **(B)** location of distal and proximal UQCRFS1 subunits (yellow ribbon) with respect to CI quinone tunnel (black dashed window). The purple box highlights the region targeted in focused 3D classification, which is the distal UQCRFS1 head domain. UQCRTT3 protein is shown in green ribbon. **(C)** Gallery display of eight 3D classes I-VIII. The distal UQCRFS1 protein and UQCRTT3 were fitted to each 3D class density map and distance measured from Fe_2S_2 cluster to heme c_1 fixed in consensus refined 3D map. Only classes V and VI display markedly different distances. **(D)** Comparison of B-state class V (left) and C-state class IV (right). B-state UQCRFS1 superposes well with stigmatellin-induced B-state UQCRFS1 from chicken $CIII_2$ (purple ribbon, PDB 3BCC). C-state UQCRFS1 superposes almost perfectly with C-state UQCRFS1 from chicken $CIII_2$ (purple ribbon, PDB 1BCC). Distance measures are shown for ciliate UQCRFS1 Fe_2S_2 to heme c_1 and b_L.

Structural basis of mitochondrial membrane bending by I-II-III_2-IV_2 supercomplex

Alexander Mühleip[1†], Rasmus Kock Flygaard[1,2†], Outi Haapanen[3], Rozbeh Baradaran[1,4], Thomas Gruhl[5], Victor Tobiasson[1], Amandine Maréchal[5,6], Vivek Sharma[3,7], Alexey Amunts[1*]

[1] Science for Life Laboratory, Department of Biochemistry and Biophysics, Stockholm University, 17165 Solna, Sweden.

[2] Current address: Department of Molecular Biology and Genetics, Danish Research Institute of Translational Neuroscience - DANDRITE, Nordic EMBL Partnership for Molecular Medicine, Aarhus University, 8000 Aarhus C, Denmark.

[3] Department of Physics, University of Helsinki, 00014 Helsinki, Finland.

[4] Current address: MRC Laboratory of Molecular Biology, Cambridge, United Kingdom.

[5] Institute of Structural and Molecular Biology, Birkbeck College, London, WC1E 7HX, UK.

[6] Institute of Structural and Molecular Biology, University College London, London, WC1E 6BT, UK.

[7] HiLIFE Institute of Biotechnology, University of Helsinki, 00014 Helsinki, Finland.

† These authors contributed equally to this work.

* Correspondence to: amunts@scilifelab.se.

SUPPLEMENTARY INFORMATION

Table of contents:

SI Figure 1. Conservation and divergence of ciliate CI

SI Figure 2. CN-PAGE gel showing active CI, CII and CIV in the final supercomplex sample

SI Figure 3. Conservation and divergence of ciliate CIV

SI Figure 4. Conservation and divergence of ciliate CIII

SI Figure 5. Ciliate $CIII_2$ heme group distances and wedged ubiquinone

SI Table 1. Data collection and model statistics

SI Table 2. List of proteins and comments

SI Video 1. Coarse-grained molecular dynamics simulation of the *T. thermophila* supercomplex.

SI Video 2. Annular lipid shell of the *T. thermophila* supercomplex.

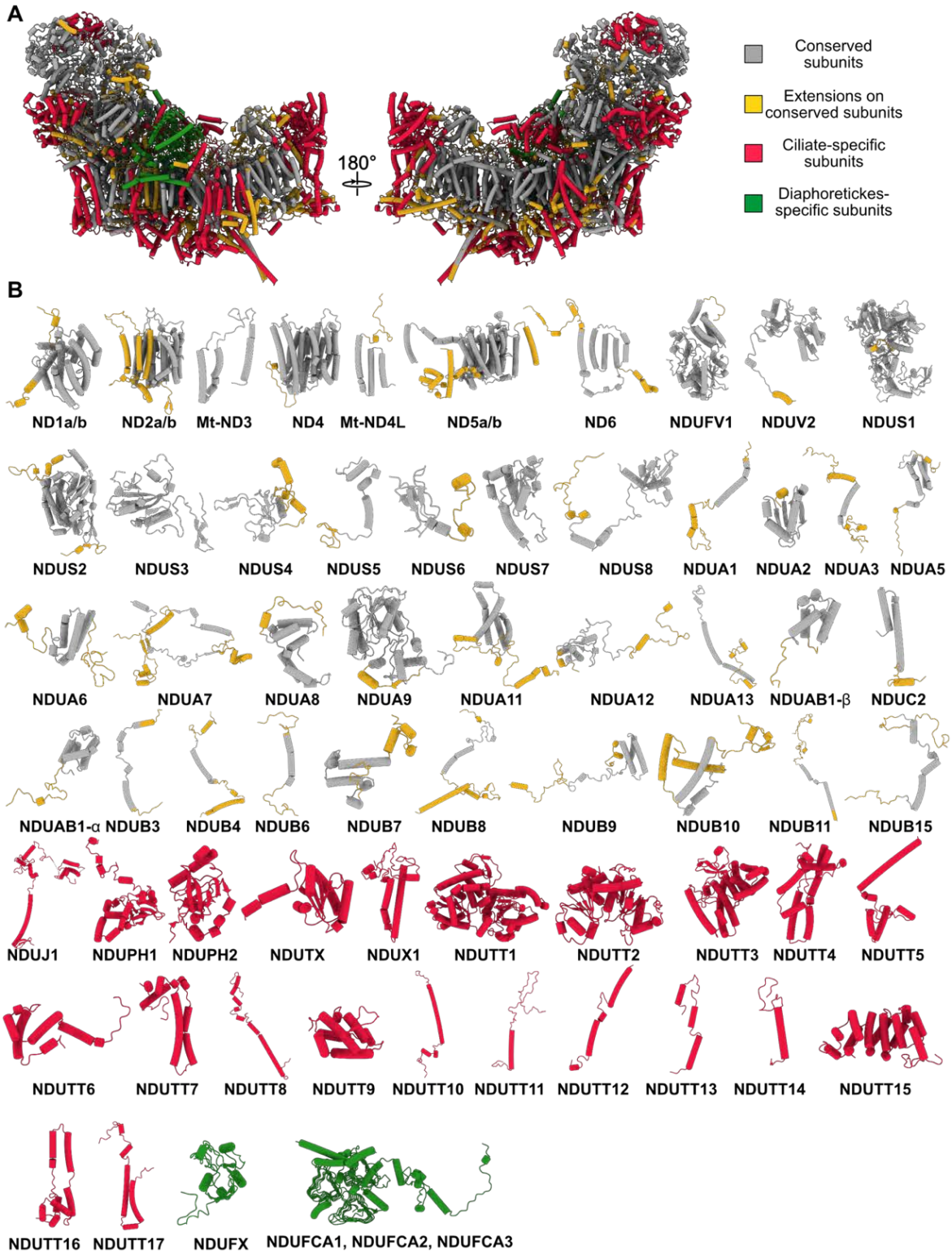

Supplementary Information Figure 1. Conservation and divergence of ciliate CI. (A) CI colored by conserved subunits (grey), extensions to conserved subunits (gold), ciliate-specific subunits (red) and Diaphoretickes-conserved subunits (green). Conservation is assessed as structural homology to mammalian CI (PDB 5LNK). Extensions and ciliate-specific subunits primarily locate to peripheral regions of the matrix arm and membrane domain. **(B)** Individual CI subunits shown as gallery with similar color coding as in A. Subunit naming as in ref (*7*).

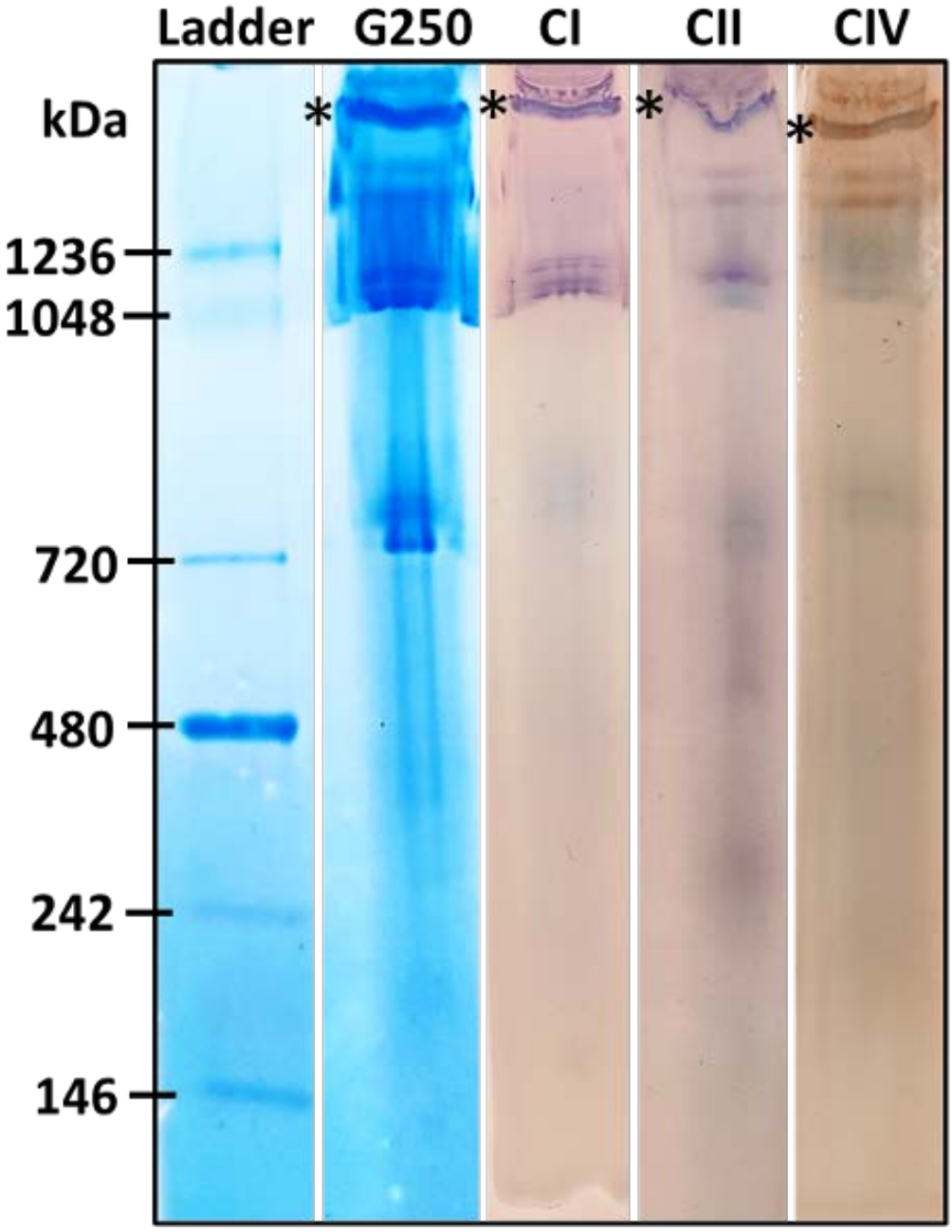

Supplementary Information Figure 2. CN-PAGE gel showing active CI, CII and CIV in the final supercomplex sample. Coomassie stained CN-PAGE and in-gel activity assay to visualise the purified I-II-III_2-IV_2 supercomplex. CN-PAGE was performed to separate protein assemblies within the final sucrose cushion sample. The ladder and G250 lanes represent the Coomassie stained molecular weight marker and final supercomplex sample, respectively. CI, CII and CIV lanes highlight those protein bands with active CI, CII (purple) and CIV (brown), respectively. The band marked with an asterisk (*) was tentatively assigned as I-II-III_2-IV_2 supercomplex.

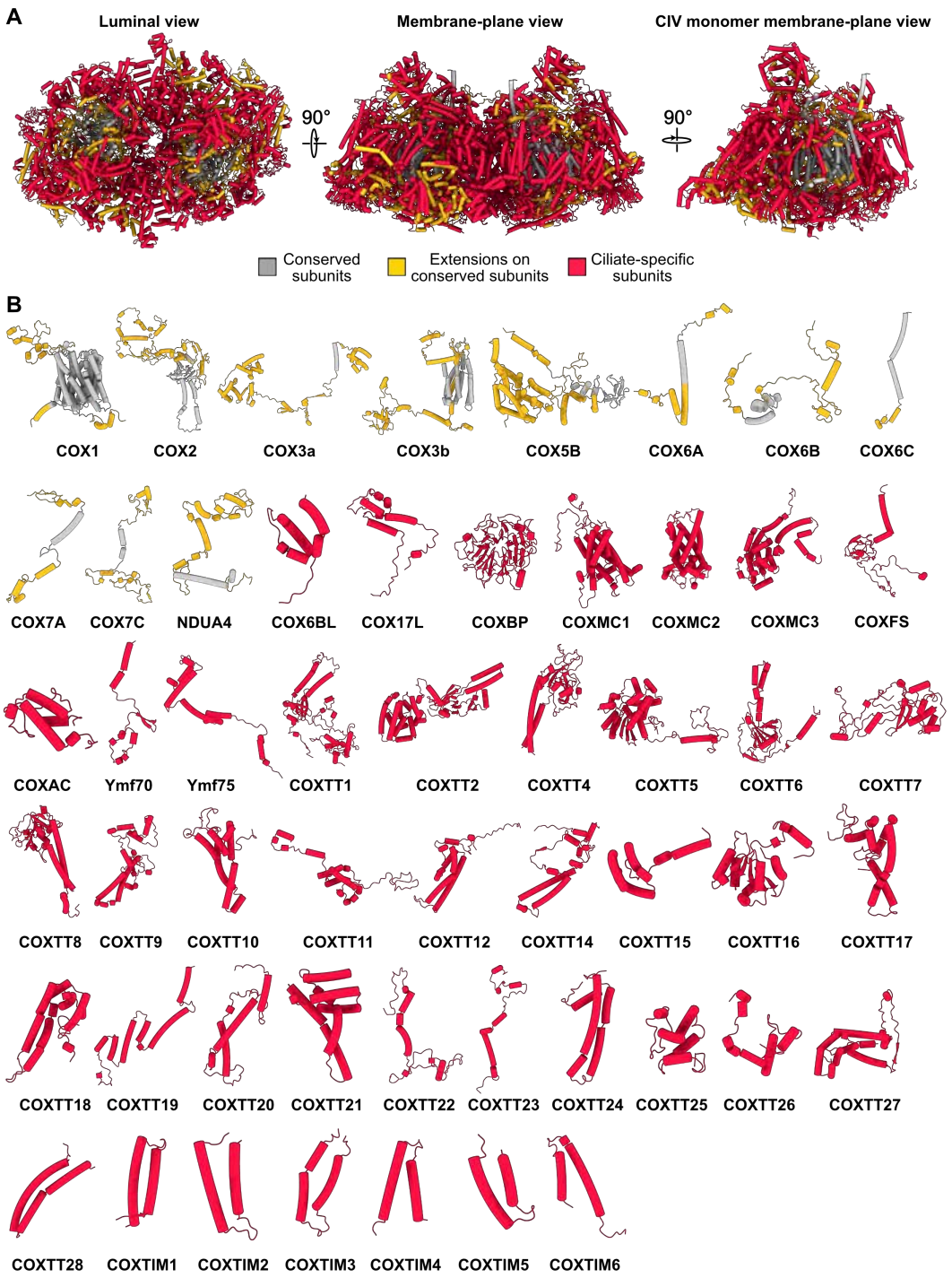

Supplementary Information Figure 3. Conservation and divergence of ciliate CIV. (A) three different views of CIV_2 colored by conserved subunits (grey), extensions to conserved subunits (gold) and ciliate-specific subunits (red). Conservation is assessed as structural homology to bovine (PDB 3X2Q) and human (PDB 5Z62) CIV structures. Right view shows a single CIV monomer assembly looking from the dimer interface. The ciliate CIV displays conserved core subunits that all contain significant extensions to the core folds. The conserved core subunits are also surrounded by ciliate-specific subunits, which make up most of the peripheral regions of the complex. **(B)** Individual CIV subunits shown as gallery with similar color coding as in A. Subunit naming is adopted from ref (*7*).

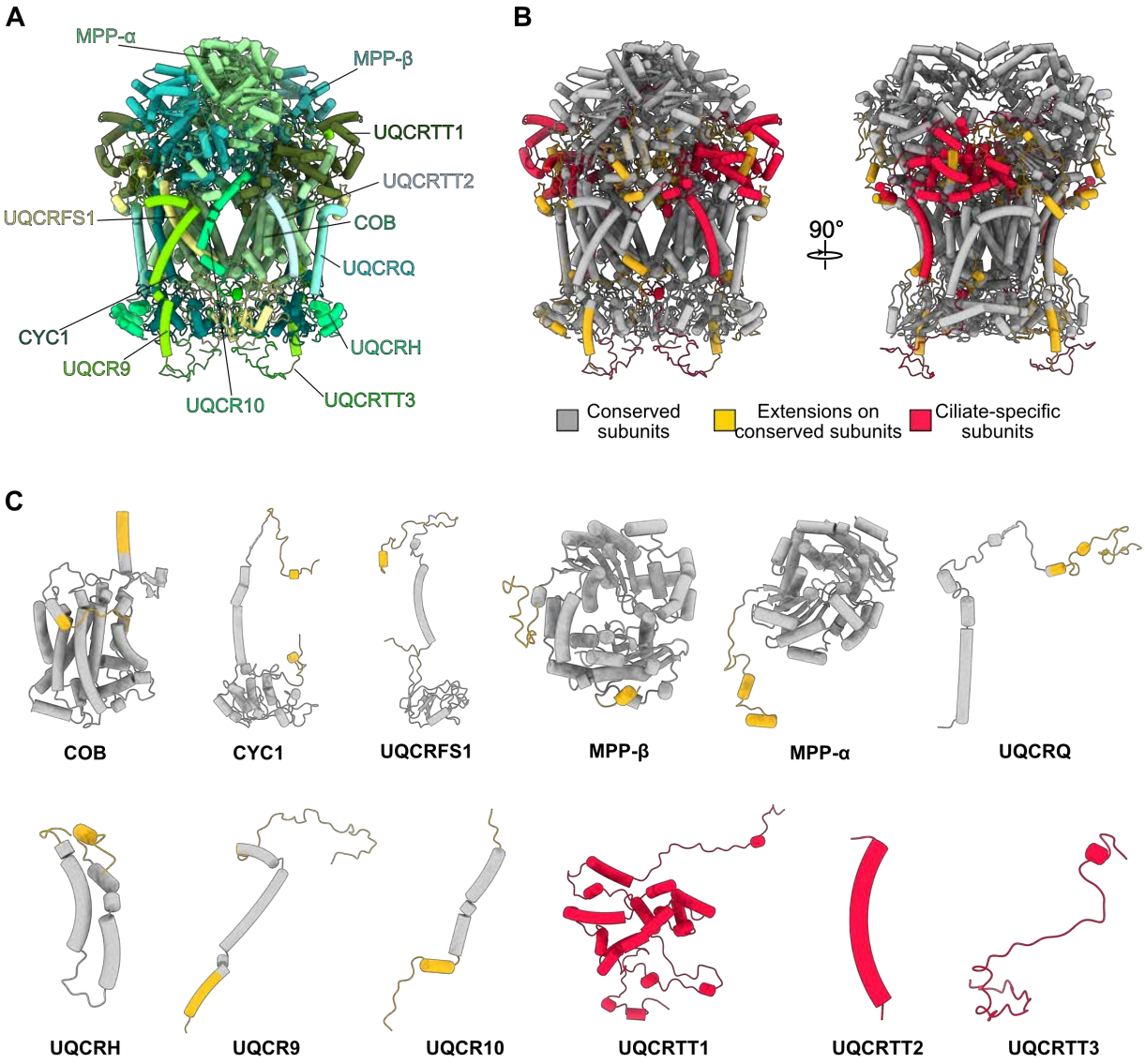

Supplementary Information Figure 4. Conservation and divergence of ciliate CIII dimer. (A) $CIII_2$ colored by subunits. **(B)** $CIII_2$ colored by conserved subunits (grey), extensions to conserved subunits (gold) and ciliate-specific subunits (red). Conservation is assessed as structural homology to bovine (PDB 5J4Z) and murine (PDB 7O3H) $CIII_2$ structures. The ciliate $CIII_2$ shows a high degree of conservation in the core subunits. **(C)** Individual CIII subunits shown as gallery with similar color coding as in B.

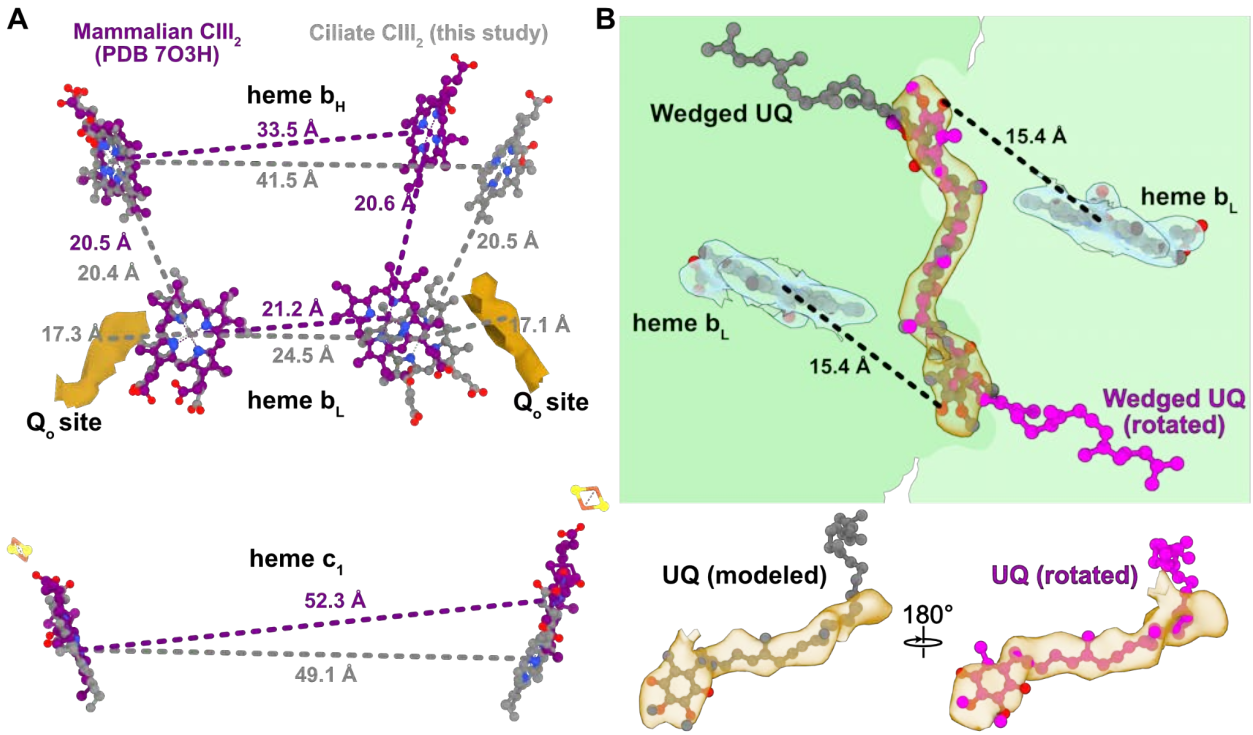

Supplementary Information Figure 5. Ciliate $CIII_2$ heme group distances and wedged ubiquinone. **(A)** Distance measures between ciliate (grey dashed lines) and mammalian (purple dashed lines) heme b_H, heme b_L and heme c_1 groups (measuring from Fe atoms) and the ciliate Q_o sites. Superposing mammalian $CIII_2$ (PDB 7O3H) on one COB chain, shows that ciliate heme b_H and heme b_L (grey sticks) are displaced further away from the symmetry-related heme groups compared to mammalian, whereas the ciliate heme c_1 groups are slightly closer. However, the distance between heme b_H and heme b_L within the same COB copy is essentially identical between ciliate and mammalian structures. Furthermore, the distance from the Q_o sites (middle of dark gold map density) to the heme b_L groups is comparable to the 16.8 Å distance between ubiquinol and the heme b_L group observed in the X-ray structure of bovine $CIII_2$ (17). **(B)** Map density (transparent gold) of the $CIII_2$ wedged ubiquinone (UQ) in COB (green) is almost rotationally symmetric around the dimer axis, showing planar density features for placement of UQ head groups equally close to the heme b_L molecules (transparent blue). We placed UQ in the orientation where the quinone fitted the map density best (grey) compared to the rotated orientation (magenta).

Supplementary Video 1. Coarse-grained molecular dynamics simulation of the *T. thermophila* supercomplex. First 800 ns of the MD simulation starting from an initially planar membrane reveals a deformation of the bilayer into a curved topology to accommodate the membrane protein complex.

Supplementary Video 2. Annular lipid shell of the *T. thermophila* supercomplex. Final frame of the coarse-grained MD-simulation with supercomplex and surrounding annular lipids shown, highlighting the curved shape of the lipid belt.

Supplementary Information Table 1. Data collection and model statistics

Data collection	CI	CII	$CIII_2$	CIV_2	$CI\text{-}II\text{-}III_2\text{-}IV_2$
Microscope	Titan Krios				
Voltage (kV)	300				
Camera	K2 Summit				
Magnification	165,000				
Exposure ($e^-/Å^2$)	30.9				
Pixel size (Å)	0.83				
Defocus range (μm)	0.6-2.6				
Movies collected	26,063				
Frames / movie	20				
Data processing					
Initial particles	1,664,103				
Final particles	138,746				
Symmetry	C1	C1	C1	C1	C1
Map resolution (Å)	2.9	2.8	2.8	2.6	2.9
- FSC threshold	0.143	0.143	0.143	0.143	0.143
B-factor sharpening	46.8	49.1	52.2	45.4	49.9
EMDB ID	EMD-	EMD-	EMD-	EMD-	EMD-
Model refinement statistics					
CC (map/model)	0.82	0.82	0.81	0.84	0.79
Resolution (map/model)	2.99	3.3	3.18	2.89	3.36
- FSC threshold	0.5	0.5	0.5	0.5	0.5
Atoms (not H)	234277	41399	94264	436066	806006
Residues	13712	2409	5438	23792	45351
Lipids/CoQ	59/0	11/1	32/3	214/8	316/12
Model B-factor ($Å^2$)					
- **Protein**	53.2	100.46	65.66	52.8	91.23
- **Ligands**	63.83	107.88	78.66	72.16	111.10
Rotamer outliers (%)	0.51%	0.62%	0.53%	1.18%	0.76
Ramachandran (%)					
- **Outliers**	0.01%	0.21%	0.00%	0.01%	0.02%
- **Allowed**	2.07%	3.28%	2.43%	1.75%	1.77
- **Favoured**	97.92%	96.51%	97.57%	98.25%	98.22
Clash score	4.12	3.91	5.68	4.22	4.63
MolProbity score	1.21	1.41	1.40	1.26	1.24
RMSD					
- **Bonds (Å)**	0.002	0.004	0.002	0.002	0.002
- **Angles (°)**	0.407	0.459	0.447	0.503	0.562
PDB ID					

Supplementary Information Table 2. List of proteins and comments

Subunit name	Gene name	UniProt ID	Encoded	Residues in total	Comments
Complex-I:					
ND1a	nad1_a	Q950Y3	mt	284	Corresponds to NuoH, Nqo8
ND1b	nad1_b	NP_149380	mt	59	Mt-ND1 C-terminal extension, separate gene
ND2a	ymf65	Q951A3	mt	360	Corresponds to NuoN, Nqo14
ND2b	nad2	Q951B2	mt	178	Mt-ND2 C-terminal extension, separate gene
Mt-ND3	nad3	Q950Z7	mt	121	Corresponds to NuoA, Nqo7
ND4	nad4	Q950X9	mt	505	Corresponds to NuoM, Nqo13
MT-ND4L	ymf58	Q950Z5	mt	116	Corresponds to NuoK, Nqo11
ND5a	nad5	Q950Z0	mt	750	Corresponds to NuoL, Nqo12
ND5b	ymf57	Q951C2	mt	100	Mt-ND5 C-terminal extension, separate gene
ND6	ymf62	Q950Y2	mt	255	Corresponds to NuoJ, Nqo10
NDUV1	TTHERM_00193910	Q23KE4	nuclear	474	Corresponds to NuoF, Nqo1
NDUV2	TTHERM_00335630	I7MEP0	nuclear	274	Corresponds to NuoE, Nqo2

NDUS1	TTHERM_00194260	Q23KA9	nuclear	718	Corresponds to NuoG, Nqo3
NDUS2	nad7	Q951B1	mt	442	Corresponds to NuoD, Nqo4
NDUS3	nad9_2	Q950Z3	mt	198	Corresponds to NuoC, Nqo5
NDUS4	TTHERM_00526930	I7MK61	nuclear	185	Corresponds to AQDQ subunit
NDUS5	TTHERM_000129647	W7X4R4	nuclear	94	
NDUS6	TTHERM_00497570	I7MK02	nuclear	132	Zinc-finger protein, contains a Zn^{2+} ion
NDUS7	nad10	Q951B4	mt	162	Corresponds to NuoB, Nqo6
NDUS8	TTHERM_00294640	I7MDW5	nuclear	236	Corresponds to NuoI, Nqo9
NDUA1	TTHERM_00455560	I7MI60	nuclear	94	
NDUA2	TTHERM_00659070	I7MA77	nuclear	103	
NDUA3	TTHERM_00148710	I7M9B3	nuclear	135	
NDUA5	TTHERM_01161000	Q23ND5	nuclear	206	
NDUA6	TTHERM_00933070	I7M2Y3	nuclear	172	
NDUA7	TTHERM_00399360	I7MIJ7	nuclear	282	
NDUA8	TTHERM_00464930	I7MMF4	nuclear	238	

NDUA9	TTHERM_00557760	I7MLH2	nuclear	362	NAD-dependent epimerase/dehydratase family protein
NDUA11	TTHERM_00945210	Q24F24	nuclear	213	
NDUA12	TTHERM_00194499	A4VDQ6	nuclear	194	
NDUA13	TTHERM_00149260	I7M2U4	nuclear	175	
NDUAB1-α	TTHERM_01005100	Q22XT6	nuclear	138	Different isoform to NDUAB1-β
NDUAB1-β	TTHERM_00470710	I7MD12	nuclear	133	Acyl carrier protein
NDUB3	TTHERM_00446569	A4VD20	nuclear	83	
NDUB4	TTHERM_00310880	I7MG29	nuclear	126	
NDUB6	TTHERM_00430000	Q231G0	nuclear	129	
NDUB7	TTHERM_00402070	I7MIM0	nuclear	120	
NDUB8	TTHERM_00481330	I7M855	nuclear	207	
NDUB9	TTHERM_00985010	Q233X7	nuclear	189	
NDUB10	TTHERM_00193750	Q23KG0	nuclear	188	
NDUB11	TTHERM_00114380	Q22Z32	nuclear	214	
NDUB15	TTHERM_000614679	-	nuclear	147	Wrong gene annotation – change translation ORF to 5′-3′ in frame 3

NDUC2	TTHERM_00160690	Q22W63	nuclear	102	
NDUCA1	TTHERM_00136440	I7M8Q7	nuclear	346	carbonic anhydrase-like protein (isoform 1)
NDUCA2	TTHERM_01005010	Q22XU5	nuclear	257	carbonic anhydrase-like protein (isoform 2)
NDUCA3	TTHERM_00541460	I7M6S0	nuclear	233	carbonic anhydrase-like protein (isoform 3)
NDUX1	TTHERM_00715850	I7LT42	nuclear	150	
NDUFX	TTHERM_00161210	Q22W11	nuclear	172	2Fe2S cluster-binding protein
NDUTX	TTHERM_01205250	Q22AI5	nuclear	166	Thioredoxin, TRX family
NDUJ1	TTHERM_00938750	Q22DR7	nuclear	317	DnaJ domain protein
NDUPH1	TTHERM_00697370	Q24C39	nuclear	251	
NDUPH2	TTHERM_00193950	Q23KE0	nuclear	189	
NDUTT1	TTHERM_00925340	Q22E24	nuclear	516	lipid A-disaccharide synthase
NDUTT2	TTHERM_01000190	Q24HK5	nuclear	333	Acyl-CoA synthetase (AMP-forming)/AMP-acid ligase II
NDUTT3	TTHERM_00268000	I7LUQ4	nuclear	311	
NDUTT4	TTHERM_00295430	I7MIE0	nuclear	212	
NDUTT5	TTHERM_00649080	I7LT77	nuclear	205	

NDUTT6	TTHERM_00334340	I7M1N8	nuclear	144	
NDUTT7	TTHERM_00637590	Q22HE4	nuclear	143	
NDUTT8	TTHERM_00006120	Q22SC4	nuclear	135	
NDUTT9	TTHERM_00653670	Q23B10	nuclear	136	
NDUTT10	TTHERM_00616320	I7MAF0	nuclear	127	
NDUTT11	TTHERM_00185570	Q22T55	nuclear	113	
NDUTT12	TTHERM_00835330	Q22E95	nuclear	93	
NDUTT13	TTHERM_00992800	Q22DC2	nuclear	73	
NDUTT14	TTHERM_00399460	I7MIK1	nuclear	71	
NDUTT15	TTHERM_00063 7389	-	nuclear	237	Wrong gene annotation – change translation ORF to 3′-5′ in frame 1 Binds ADP-Mg^{2+}
NDUTT16	TTHERM_00124 3407	W7XFJ5	nuclear	119	Is required for I-IV_2 interface stability. Stabilises ND5a Nt extension.
NDUTT17	TTHERM_00053 2499	-	nuclear	125	Wrong gene annotation – change translation ORF to 3′-5′ in frame 2
Complex-II:					
SDHA	TTHERM_00047080	Q23DI3	nuclear	636	

SDHB	TTHERM_00241700	I7M403	nuclear	312	
SDHC	TTHERM_00387120	Q23RH8	nuclear	60	
SDHD	AF396436.1 (mt-genome sequence)	-	mt	43	Gene lies between ymf66 and ymf76 on mtDNA. Translation 3′-5′ in frame 1
SDHTT1	TTHERM_00571650	Q24I09	nuclear	322	contains heme c
SDHTT2	TTHERM_00532090	Q248F8	nuclear	296	
SDHTT3	TTHERM_00283850	I7MEX7	nuclear	198	
SDHTT4	TTHERM_00658950	I7LX66	nuclear	195	Diphthamide synthesis protein
SDHTT5	TTHERM_00601860	Q22YL0	nuclear	114	
SDHTT6	TTHERM_00626980	Q23S01	nuclear	103	
SDHTT7	TTHERM_00713350	Q24CW6	nuclear	93	
SDHTT8	TTHERM_000287919	W7XBF5	nuclear	89	
SDHTT9	TTHERM_00637670	Q22HD6	nuclear	76	
SDHTT10	TTHERM_001034353	W7XF00	nuclear	62	
SDHTT11	DY684362.1 (EST, mRNA sequence)	-	nuclear	46	Gene translation should be 3′-5′ in frame 1
Complex-III:					

MPP-β	TTHERM_00502380	I7MGU2	nuclear	513	
MPP-α	TTHERM_00836690	I7MJ25	nuclear	482	
COB	cob	Q950Z1	mt	426	contains heme bL and bH
CYC1	TTHERM_00918500	Q24IM5	nuclear	319	Contains heme c
UQCRFS1	TTHERM_00295080	I7MIC7	nuclear	269	Contains 2Fe2S cluster
UQCRH	TTHERM_00194690	Q23K66	nuclear	86	cytochrome bc1 hinge proteins
UQCRQ	TTHERM_00765330	I7M484	nuclear	130	
UQCR9	TTHERM_00456790	I7MM45	nuclear	119	
UQCR10	TTHERM_00218930	I7MFL6	nuclear	62	
UQCRTT1	TTHERM_00382330	Q23F81	nuclear	328	
UQCRTT2	EV837551.1 (EST, mRNA sequence)	-	nuclear	41	Gene translation should be 5′-3′ in frame 3
UQCRTT3	-	-	-	66	Unidentified subunit
Complex-IV:					
COX1	cox1	Q950Y4	mt	688	

COX2	cox2	Q950Y9	mt	604	
COX3a	ymf67	Q950Y7	mt	453	structurally replaces H1 of COX3
COX3b	ymf68	Q950Y6	mt	594	
COX5B	TTHERM_00378620	Q23FF5	nuclear	637	
COX6A	TTHERM_000723218	W7XCY5	nuclear	130	
COX6B	TTHERM_00568030	Q24I72	nuclear	230	
COX6C	TTHERM_00046170	Q23DS4	nuclear	103	
COX7A	TTHERM_00151250	I7MGF9	nuclear	133	
COX7C	TTHERM_000470561	W7X287	nuclear	236	
COX6BL	TTHERM_00218340	I7LVX0	nuclear	88	
COX17L	TTHERM_01043280	Q22CI1	nuclear	990	CTF/NF-I domain-containing protein
NDUA4	TTHERM_001001528	W7WZP1	nuclear	220	(Named COXTT13 in Zhou et al.)
COXMC1	TTHERM_00127269	A4VDV3	nuclear	346	Oxoglutarate/malate translocator protein
COXMC2	TTHERM_00621600	Q23M99	nuclear	318	2-oxoglutarate/malate carrier protein
COXMC3	TTHERM_00112650	Q22ZA6	nuclear	330	

COXBP	TTHERM_00016360	Q22RF2	nuclear	685	BBC53 chromosome condensation regulator RCC1
COXTIM1	TTHERM_000528460	W7X3D6	nuclear	72	Tim10/DDP family zinc finger proteins
COXTIM2	TTHERM_000703379	W7XDM6	nuclear	72	part of TIM9.10 hexamer
COXTIM3	TTHERM_00433490	Q231A8	nuclear	93	part of TIM9.10 hexamer
COXTIM4	TTHERM_01289060	Q22A35	nuclear	68	part of TIM9.10 hexamer
COXTIM5	TTHERM_00028510	Q22N23	nuclear	81	part of TIM9.10 hexamer
COXTIM6	TTHERM_00805850	Q233U0	nuclear	72	part of TIM9.10 hexamer
COXFS	TTHERM_00133510	I7M8P0	nuclear	188	Fe-binding zinc finger CDGSH type protein
COXAC	TTHERM_00695750	Q24C97	nuclear	127	
Ymf70	ymf70	Q950Y0	mt	89	
Ymf75	ymf75	Q951A7	mt	190	
COXTT1	TTHERM_00361490	Q22PJ5	nuclear	490	
COXTT2	TTHERM_00721790	Q22FX8	nuclear	473	Protein phosphatase 2C
COXTT4	TTHERM_00338280	I7M1Q4	nuclear	402	SURF1 family protein
COXTT5	TTHERM_00046440	Q23DP7	nuclear	385	TraB family protein

COXTT6	TTHERM_00047230	Q23DG8	nuclear	348	
COXTT7	TTHERM_00675650	Q23DZ5	nuclear	318	
COXTT8	TTHERM_00070850	I7LTZ4	nuclear	318	SURF1 family protein
COXTT9	TTHERM_00525160	I7LY65	nuclear	252	
COXTT10	TTHERM_00420130	I7MD70	nuclear	234	
COXTT11	TTHERM_000939159	W7X4J9	nuclear	231	
COXTT12	TTHERM_00455090	I7M3P9	nuclear	215	
COXTT14	TTHERM_00530650	I7LZX8	nuclear	210	
COXTT15	TTHERM_00641250	Q23F08	nuclear	193	
COXTT16	TTHERM_00218840	I7M8Y9	nuclear	175	AAA protein fold
COXTT17	TTHERM_00049040	Q23D87	nuclear	173	
COXTT18	TTHERM_00218570	I7MKT6	nuclear	173	
COXTT19	TTHERM_00433830	Q230X6	nuclear	170	
COXTT20	TTHERM_00794470	Q23VY4	nuclear	158	
COXTT21	TTHERM_00938940	Q22DP8	nuclear	154	
COXTT22	TTHERM_00691100	I7MFV5	nuclear	149	

COXTT23	TTHERM_00666370	Q23TE5	nuclear	124	
COXTT24	TTHERM_00161000	Q22W32	nuclear	122	
COXTT25	TTHERM_00151580	I7M9E7	nuclear	105	
COXTT26	TTHERM_00485790	I7LTF1	nuclear	90	
COXTT27	TTHERM_000302101	W7XDH2	nuclear	212	(Including subunit COXTT3 in Zhou et al.)
COXTT28	TTHERM_000933397	W7X912	nuclear	171	